TU Delft

Delft University of Technology

Optimal Control for Distributed Aeroelastic Morphing Structure with Uncertainties and Imperfections

Mkhoyan, T.; Wang, Xuerui; De Breuker, R.

DOI
10.2514/6.2024-0832

Publication date
2024

Document Version
Final published version

Published in
Proceedings of the AIAA SCITECH 2024 Forum

Citation (APA)
Mkhoyan, T., Wang, X., & De Breuker, R. (2024). Optimal Control for Distributed Aeroelastic Morphing Structure with Uncertainties and Imperfections. In *Proceedings of the AIAA SCITECH 2024 Forum* Article AIAA 2024-0832 (AIAA SciTech Forum and Exposition, 2024). American Institute of Aeronautics and Astronautics Inc. (AIAA). https://doi.org/10.2514/6.2024-0832

Important note
To cite this publication, please use the final published version (if applicable).
Please check the document version above.

Copyright
Other than for strictly personal use, it is not permitted to download, forward or distribute the text or part of it, without the consent of the author(s) and/or copyright holder(s), unless the work is under an open content license such as Creative Commons.

Takedown policy
Please contact us and provide details if you believe this document breaches copyrights.
We will remove access to the work immediately and investigate your claim.

This work is downloaded from Delft University of Technology.
For technical reasons the number of authors shown on this cover page is limited to a maximum of 10.

AIAA SciTech Forum
8-12 January 2024, Orlando, FL
AIAA SCITECH 2024 Forum

10.2514/6.2024-0832

Optimal Control for Distributed Aeroelastic Morphing Structure with Uncertainties and Imperfections

Tigran Mkhoyan*, Xuerui Wang†, Roeland De Breuker‡
Delft University of Technology, Delft, The Netherlands

This research takes a further step towards the development of an autonomous aeroservoelastic wing concept with distributed flaps. The wing demonstrator, developed within the TU Delft SmartX project, aims to demonstrate in-flight performance optimization and multi-objective control using an over-actuated wing design. To address the challenges posed by the aeroelastic system's nonlinearities and uncertainties, this paper employs an optimal control method relying on solving the State-Dependent Riccati Equation (SDRE). Geometrical nonlinearities, introduced in the form of plunge and torsion stiffness, make the system state-dependent and unsuitable for linear control methods. Additionally, a backlash model is incorporated to represent the uncertainty of the actuation system. The control strategy is implemented in a multi-objective manner to perform maneuver and gust load alleviation while accounting for the nonlinearities and uncertainties using the SDRE control. Firstly, a numerical sample case is investigated involving a state-dependent and highly non-linear canard aircraft configuration, to assess the ability of the SDRE control method. Then, in a numerical experiment, the effectiveness of the control strategy is evaluated through the nonlinear aeroelastic model. Evaluations are made on the practicality of the control approach, laying a foundation for future static and dynamic wind tunnel experiments with the SmartX-Neo demonstrator.

Downloaded by Technische Universiteit Delft on January 5, 2024 | http://arc.aiaa.org | DOI: 10.2514/6.2024-0832

I. Abstract

The advancements in aircraft materials, manufacturing technology, control algorithms, and hardware design allow the development of increasingly flexible aircraft concepts. Generally, flexibility comes as a side effect of lighter aircraft design and must be considered adequately. However, a more natural approach is to utilize the flexibility for the benefit of better performance, much like it is seen in nature with wing morphing for better gliding performance [1, 2]. As in nature, flexible wing concepts have been evolving since the early years of aviation.

One of the well-documented examples was the active roll control of the Wright Flyer, the first successful heavier-than-air powered aircraft. In this lightweight design, the lateral stability was ensured by wing twist-warping [3]. This was possible because the flexible fabric-wrapped structure was well-suited for morphing. As the flight speeds and loads were increased with the advancement of flight, a stiffer wing was required to fulfil structural requirements and overcome aeroelastic instabilities. As a result, the considerably more rigid wing design - generally optimized for cruise conditions - is faced with a compromised performance in other flight conditions. To harness the potential of a flexible wing, two design choices are possible: active morphing design and conventionally flapped distributed wing designs. Both design concepts can allow the lift distribution to be tailored actively, potentially reducing this performance loss and improving aircraft performance across the flight envelope. Furthermore, both design concepts can be distributed and modular (i.e., having multiple flaps along the span), mimicking the distributed nature of feathers found in avian biology. However, such flexible and modular concepts involve complex designs which may come with inherent non-linearities, further exacerbated by aero-elastic coupling or uncertainties present in actuator systems such as backlash [4, 5].

The control of such flexible wing systems with nonlinearities and uncertainties poses significant challenges. One approach that has been extensively studied is the use of the State-Dependent Riccati Equation (SDRE) control technique. SDRE control has been applied successfully to various aeroelastic systems, including aircraft wings. A literature review reveals several notable applications of SDRE control in addressing system nonlinearities and uncertainty of actuator

*Researcher, Faculty of Aerospace Engineering, Department of Aerospace Structures and Materials, T.Mkhoyan@tudelft.nl, P.O. Box 5058, 2600GB Delft, The Netherlands.

†Assistant Professor, Faculty of Aerospace Engineering, Department of Aerospace Structures and Materials & Department of Control and Operations, X.Wang-6@tudelft.nl, P.O. Box 5058, 2600GB Delft, The Netherlands, Senior Member AIAA.

‡Associate Professor, Faculty of Aerospace Engineering, Department of Aerospace Structures and Materials, R.DeBreuker@tudelft.nl, P.O. Box 5058, 2600GB Delft, The Netherlands, Associate Fellow AIAA.

Copyright © 2024 by Tigran Mkhoyan. Published by the American Institute of Aeronautics and Astronautics, Inc., with permission.

dynamics. For instance, in the work of Bhoir et al. [6], SDRE control was employed to mitigate the adverse effects of nonlinearities in aeroelastic systems, resulting in improved flutter suppression performance. Additionally, Li et al. [7] proposed an SDRE-based control approach that effectively handled the uncertainties associated with actuator dynamics in an aeroelastic airfoil section. Several studies investigated SDRE control for general Another study investigated SDRE tracking for a hydraulic actuation system subject to nonlinearities, demonstrating general effectiveness to uncertain actuator dynamics [8]. These studies highlight the effectiveness of SDRE control in addressing the challenges posed by nonlinearities and uncertainties in aeroelastic systems.

While active morphing benefits aerodynamic efficiency, the morphing mechanism required for smooth shape control generally needs larger actuation forces and a more complex design. In our previous study, we have demonstrated a seamless morphing wing concept [9, 10], the SmartX-Alpha, capable of performing objectives such as shape control, drag minimization, and simultaneous gust and maneuver load alleviation [4]. This design showed a significant advantage over previous morphing concepts, allowing the lift distribution to be controlled locally by individually adjusting the camber and twist of each morphing module. However, the relatively high loads on actuators make large-area continuous morphing surfaces less appropriate in fast control tasks, such as gust load alleviation and flutter suppression. The SmartX-Neo research aims to address this gap and investigate the potential of *discrete morphing* with conventionally free hinged flaps. The benefit is significantly lower actuation forces and a simpler actuation mechanism. This initiated the development of the SmartX-Neo wing demonstrator concept. This paper describes the design and aeroelastic analysis of the wing demonstrator. Furthermore, the development and integration of the wing concept are discussed for future static and dynamic wind-tunnel experiments at the Open Jet Facility (OJF) of Delft University of Technology.

This paper is structured as follows. In Sec. II.A, the aim of the SmartX project and the objectives of the SmartX-Neo are presented. Section II.B discusses the design methodology of the SmartX-Neo wing and the envisioned aircraft platform. The aeroservoelastic model and the control design are presented in Sec. III and Sec. III.C. The nonlinear stiffness and the actuator model are presented in Sec. III.B.1 and III.B.2. Sec. IV presents two numerical experiments. First, a sample case was investigated in Sections IV.A and V.A to demonstrate the ability of the SDRE control approach applied to stabilize a non-linear aircraft model. Then, the effectiveness of the control strategy is evaluated on the non-linear aeroelastic SmartX-Neo model subject to gust disturbance in Sec. V and actuator imperfection. Finally, the conclusions are presented in Sec. VI.

Downloaded by Technische Universiteit Delft on January 5, 2024 | http://arc.aiaa.org | DOI: 10.2514/6.2024-0832

II. Design Methodology

In the following sections, the design methodology of the SmartX-Neo is presented. In Sec. II.A, the aim of the SmartX project and the objectives of the SmartX-Neo are presented. Section II.B discusses the wing and aircraft planform design. Section II.C discussed briefly the manufacturing philosophy of the hardware demonstrator and integration of sensors and actuation systems.

A. SmartX Philosophy

In the SmartX project, the aim is to achieve in-flight performance optimization through the integration of control, sensing, and morphing design. The project focuses on several objectives, including drag optimization, load alleviation, flutter suppression, and shape control [4]. The initial development within the project resulted in the SmartX-Alpha, a smart morphing wing capable of continuous active morphing with distributed Translation Induced Camber (TRIC) for local control of lift distribution and optimal lift-to-drag ratio [11]. However, the actuation bandwidth limitations of the morphing concept hindered faster objectives such as flutter suppression. To address this gap, the SmartX-Neo concept was developed, featuring discrete morphing with conventionally hinged flaps and a simpler actuation mechanism. The SmartX-Neo aims to investigate the benefits of discrete morphing, conventionally hinged flaps, over-actuated wing concepts, and actuation speed on control objectives. By comparing discrete morphing with smooth morphing, assessing the advantages of conventionally hinged flaps, and exploring advanced control methods with over-actuated wings, the SmartX-Neo project aims to advance the understanding of aeroelastic control and actuation system design. Figure 1 illustrates a comparison of the objectives between the SmartX-Alpha and the SmartX-Neo.

B. Planform Design and Analysis

The wing design of the SmartX-Neo was evaluated using an aerodynamic model built with XFLR5 [12] and a Finite Element Model (FEM) constructed using ABAQUS [13] to represent the wing's structure. The planform design aimed to investigate the benefits of advanced control methods for over-actuated aeroelastic wings and integration into an

Downloaded by Technische Universiteit Delft on January 5, 2024 | http://arc.aiaa.org | DOI: 10.2514/6.2024-0832

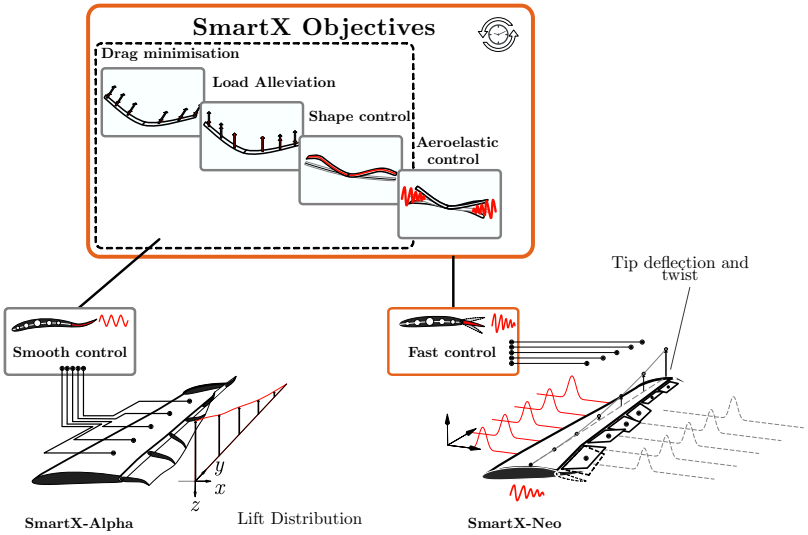

Fig. 1 Comparison of the objectives of the SmartX-Alpha and SmartX-Neo.

autonomous glider platform. The wing profile NACA0015 was selected for a good trade-off between aerodynamic performance and required structural components and instrumentation volume. The wing's span was set at 1.7 m considering manufacturing constraints. Preliminary design and assessment of the suitable flight platform and glider configuration were conducted, including the elevator and vertical stabilizer. The elevator and vertical stabilizer were sized relative to the main wing, ensuring a balanced design. Steady-state stability analysis was performed to determine the relative placement of the wings and the body, resulting in the determination of the center of gravity (COG) and neutral point. Additional details of the planform design and parameters can be found in Appendix A and Table 1.

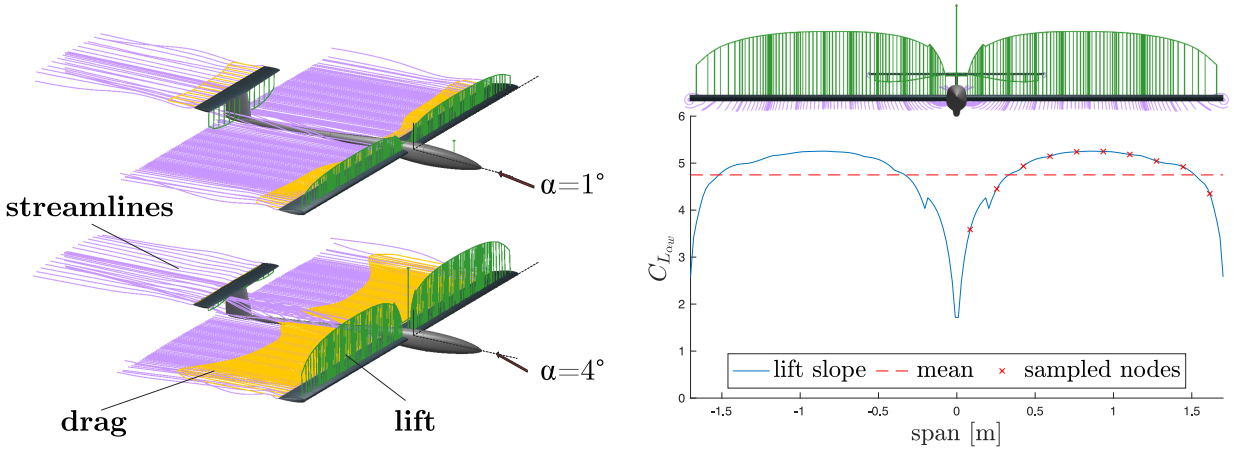

(a) Aerodynamic analysis for conditions $\alpha = 4°$ and $\alpha = 1°$, at $V_\infty = 35$ m/s.

(b) Lift slope $C_{L_{\alpha_w}}$ distribution main wing used in the aeroservoelastic model, $V_\infty = 35$ m/s, $\alpha = 4°$.

Fig. 2 Aerodynamic analysis and wing lift distribution.

To assess the aerodynamic load on the wing structure and evaluate the lift generated by the flaps, an aerodynamic model was built using XFLR5. This model employed the Vortex Lattice Method (VLM) and the 3D panel method based on XFOIL [12, 14]. The analysis was performed at a cruise condition of $V_\infty = 35$ m/s and $\alpha = 4°$. The resulting lift distribution along the wing span and torque on the flap hinge were obtained from the aerodynamic analysis. The wing's aerodynamic mesh consisted of 2600 VLM panels and, 5225 3D panels. The analysis included a type 1 (fixed speed) viscous analysis with a specified viscosity. Figure 2 presents the aerodynamic analysis results, showcasing the

lift distribution along the span and the streamlines at different angles of attack.

Overall, the design methodology of the SmartX-Neo was focused on the integration of control, sensing, and morphing design to achieve in-flight performance optimization. The wing's planform design, based on preliminary assessments and evaluations, aims to explore advanced control methods for over-actuated aeroelastic wings. Aerodynamic analysis using XFLR5 provides insights into the wing's performance and lift distribution, contributing to the design process.

C. Manufacturing philosophy

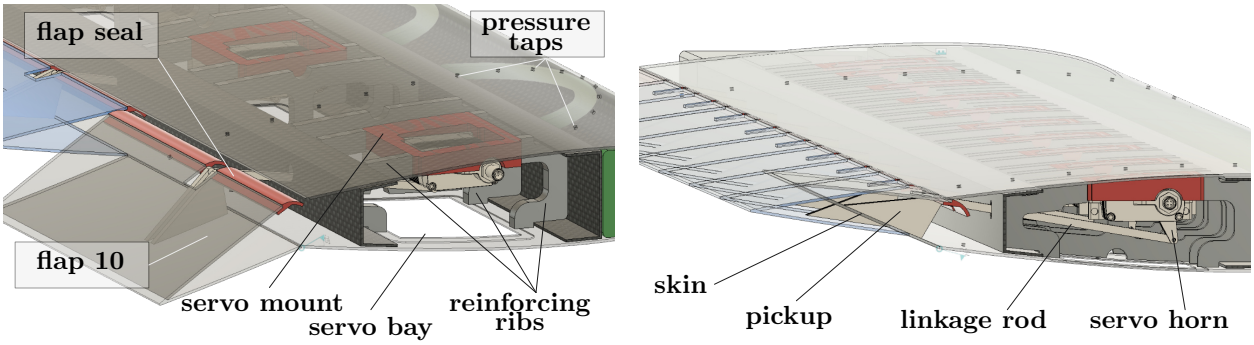

(a) Flap close-up view. **(b) Flap side view.**

Fig. 3 Overview of the actuation mechanism.

The manufacturing philosophy of the SmartX-Neo project involved the construction of a composite wing demonstrator with a wing-box structure and an integrated actuation mechanism. The manufacturing process consisted of multiple steps and the assembly and integration of various components.

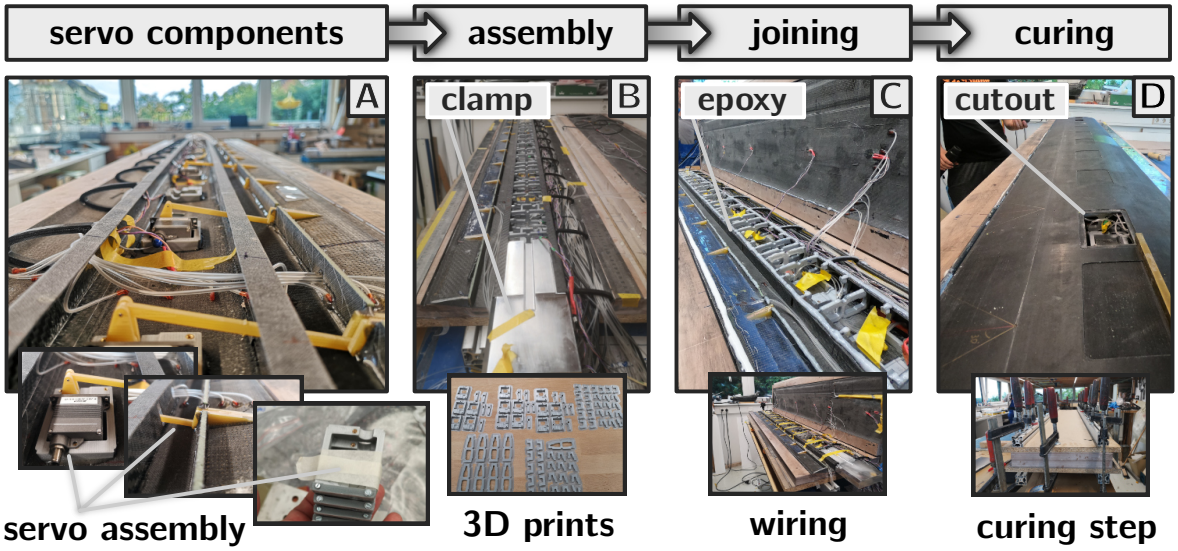

Fig. 4 Assembly integration process.

The composite wing design was divided into four parts: the top skin, bottom skin, wing box structure, and distributed flap modules. A mold was created using Polyurethane based SikaBlock with a density of 650 kg/m^3. The wing skins were manufactured using three layers of 160 g/m^2 carbon fiber and an additional layer of 40 g/m^2 fiberglass for a smooth surface finish. The skins were cured using the hand layup technique and vacuum bagged in the top and bottom molds. The spars, made of two layers of 160 g/m^2 carbon fiber, were cured separately and then assembled into the main wing structure. Foam-reinforced Kevlar material and Herex foam strips were used to enhance stiffness. The integration

Downloaded by Technische Universiteit Delft on January 5, 2024 | http://arc.aiaa.org | DOI: 10.2514/6.2024-0832

process focused on assembling the various components of the wing. The actuation mechanism, designed to be fully integrated inside the wing, was assembled after joining the top and bottom parts of the wing. 3D-printed parts made of polylactic acid (PLA) were used in the assembly process. A supporting rib structure was added near the cutouts to resist buckling.

Sensor and module integration were also key aspects of the manufacturing process. Strain gauges, fiber optics sensors, and pressure taps were installed at various locations on the wing to measure strain, twist, and pressure distribution. The tubing for pressure measurement was guided through the wing root and D-box area. Additionally, flexible feather-like patches were integrated between the modules to improve the smoothness and aerodynamic properties of the flaps. The control architecture of the glider platform, responsible for the controller and sensor data processing, followed a distributed data-sharing approach based on decentralized communication principles. This architecture facilitated the integration of over-actuated wing systems and a multitude of sensors. It allowed for parallel integration of hardware and software components in various programming languages and communication protocols, enabling real-time operation.

Downloaded by Technische Universiteit Delft on January 5, 2024 | http://arc.aiaa.org | DOI: 10.2514/6.2024-0832

III. Aeroservoelastic Model

An aeroservoelastic model is developed in Matlab/Simulink to access actuator requirements concerning the expected dynamic response of the wing demonstrator and develop a controller capable of fulfilling the objectives of the SmartX-Neo. The model is adapted from [15] and represents a coupled unsteady aeroservoelastic model, trimmed at an air density $\rho_{\text{air}} = 1.225$ kg/m^3 and free stream velocity $V_\infty = 35$ m/s. It is composed of ten aerodynamic strips placed at equal distances, and the span corresponds to the number of flaps.

A. Model structure

To study the behavior of the aeroelastic wing, the wing structure is modeled as a linear Euler-Bernoulli beam. Each actuator (flap) is modeled as a second-order mass-spring-damping system, with a hinge moment control input M_f^{act}. The clamped beam-flap model has four degrees of freedom at each node, represented by the state vector $\mathbf{x}_s = \begin{bmatrix} w & \phi & \theta & \beta \end{bmatrix}^\mathsf{T}$. Where, w, ϕ, θ, represent the transverse displacement ($\downarrow +$), bending ($\circlearrowleft +$), torsion ($\circlearrowleft +$) and β is the flap rotation angle ($\circlearrowleft +$). The dynamics for the clamped beam are given by:

$$\mathbf{M}_s\ddot{\mathbf{x}}_s + \mathbf{C}_s\dot{\mathbf{x}}_s + \mathbf{K}_s\mathbf{x}_\mathbf{s} = \begin{bmatrix} \mathbf{F_r} & \mathbf{F_{ext}} \end{bmatrix} \tag{1}$$

Where $\mathbf{M}_s, \mathbf{C}_s, \mathbf{K}_s$ and structural mass damping and stiffness matrices, respectively. On the right-hand side, $\mathbf{F_r}$ and $\mathbf{F_{ext}}$ are the wing root reaction forces and the distributed external forces. The wing root reaction forces are, the shear force, the root bending moment, and the torsion moment contained in vector $\mathbf{F_r} = \begin{bmatrix} F_w & M_\phi & M_\theta \end{bmatrix}^\mathsf{T}$. Structural damping is added proportionally to the stiffness matrix, though $\mathbf{C}_s = k_s\mathbf{K}_s$, where $\mathbf{C}_s$ is the damping matrix and k_s a scaling factor.

In Eq. (1) beam structural mass and stiffness matrices $\mathbf{M}_s$ and $\mathbf{K}_s$ are augmented to include the effect of the flap, yielding $\mathbf{M}_s^{\text{aug}}$ and $\mathbf{K}_s^{\text{aug}}$, as follows:

$$\mathbf{M}_s^{\text{aug}} = \begin{bmatrix} \begin{bmatrix} & \mathbf{M}_s & \end{bmatrix} & \begin{matrix} S_\beta \\ 0 \\ I_\beta + b(c-a)S_\beta \end{matrix} \\ \begin{matrix} S_\beta & 0 & I_\beta + b(c-a)S_\beta \end{matrix} & I_\beta \end{bmatrix}, \qquad \mathbf{K}_s^{\text{aug}} = \begin{bmatrix} \begin{bmatrix} & \mathbf{K}_s & \end{bmatrix} & \begin{matrix} 0 \\ 0 \\ 0 \end{matrix} \\ \begin{matrix} 0 & 0 & 0 \end{matrix} & K_\beta \end{bmatrix} \tag{2}$$

In Eq. (2), the flap angle state β is coupled with the main beam structure through inertia couplings and a rotational spring, serving as actuator stiffness. The measurable outputs are the shear force, the root bending moment, and the node displacements in the heave direction w. In total, ten nodes are movable; the first node denotes as 0^{th}, is the reference node at the root (clamped). The remaining nodes are labeled 1-10^{th} and correspond to the center location of each flap as shown in Fig. 5.

In total, ten nodes are movable; the first node denoted as 0^{th}, is the reference node at the root (clamped). The remaining nodes are labeled 1-10^{th} and correspond to the center location of each flap as shown in Fig. 5.

1. Aerodynamics

Because of the high aspect ratio of the wing, the two-dimensional strip theory was adopted where the unsteady aerodynamic forces on each strip are represented in a time-domain formulation, equivalent to Theodorsen's frequency-domain model [16]. The time-domain formulation used in this study is the indicial function approximation by Leishman [17].

Referring to Ref. [17] four lag states are introduced for each aerodynamic strip to model the circulatory part of the aerodynamic response. Similar to the structural part, the aerodynamic state vector is represented by $\mathbf{x}_a = \begin{bmatrix} w & \phi & \theta & \beta & z_i \end{bmatrix}^\mathsf{T}$. Where the latter entry is the lag states. The aerodynamic force vector, $\mathbf{F}_a$, is defined as:

$$\mathbf{F}_a = \mathbf{M}_a \ddot{\mathbf{x}}_a + \mathbf{C}_a \dot{\mathbf{x}}_a + \mathbf{K}_a \mathbf{x}_s + \mathbf{K}_z z_i \tag{3}$$

2. Couplings

The coupling of the structural and the aerodynamic models is described in [15]. The full aeroservoelastic model contains the following states:

$$\mathbf{x}_{ae} = \begin{bmatrix} \dot{\mathbf{x}}_s & \mathbf{x}_s & z_1 & z_2 & z_3 & z_4 \end{bmatrix}^\mathsf{T} \tag{4}$$

where $\mathbf{x}_s$ is the structural state vector, representing the nodal degrees-of-freedom for each of the 11 nodes; z_1, z_2, z_3, z_4 are the aerodynamic lag states.

An overview of the coordinate system, nodes, and axis definitions of the aeroelastic system is presented in Fig. 5. Here O_w represents the right-wing frame.

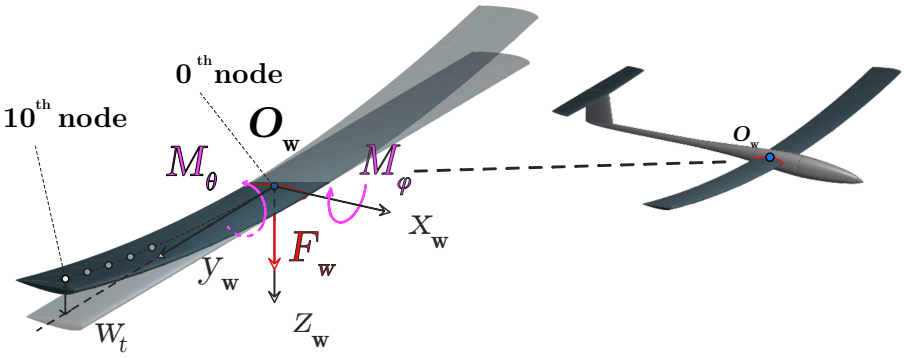

Fig. 5 Reference frames, axis definitions, and degrees of freedom of the aeroelastic system (the right wing).

3. Gust model

Initial assessment of the dynamic response is performed with a simplified gust model, a "1-cosine" gust profile, assumed to be uniform across the span and represented as an increment in α:

$$\alpha_g(t) = W_g \left(1 - \cos\left(\omega_g t\right)\right) \tag{5}$$

where W_g is the gust magnitude, and ω_g is the gust frequency in radians, calculated as $\omega_g = 2\pi f_g$. Here, f_g is the gust frequency in Hz. For this study, gust is assumed to be uniform along wing span.

B. System non-linearities

1. Geometric non-linearities

In the definition of the structural matrices, non-linearity is assumed in the torsional (pitch) and transverse displacement (plunge) of the structural stiffness parameters. Various models are adopted in literature, one of the common approaches describing polynomial nonlinearity of stiffness parameters [18]:

Downloaded by Technische Universiteit Delft on January 5, 2024 | http://arc.aiaa.org | DOI: 10.2514/6.2024-0832

$$\mathbf{K}_w(w) = \underbrace{(c_1)}_{\mathbf{K}_{w_1}} + \underbrace{(c_1 c_2 w)}_{\mathbf{K}_{w_{nl}}} \tag{6}$$

Here the plunge stiffness is a function of the transverse displacement with linear and non-linear parts, K_{w_1} and $K_{w_{nl}}$, respectively. The transverse displacement is a function of time.

The nonlinearity in the torsional stiffness parameter is described as a quartic polynomial:

$$\mathbf{K}_\theta(\theta) = \underbrace{(c_3)}_{\mathbf{K}_{\theta_1}} - \underbrace{(c_3 c_4 \theta + c_3 c_5 \theta^2 + c_3 c_6 \theta^3 + c_3 c_7 \theta^4)}_{\mathbf{K}_{\theta_{nl}}} \tag{7}$$

Here, similarly, the torsional stiffness $\mathbf{K}_\theta(\theta)$ is state dependent in θ and consists of a linear and non-linear part, K_{θ_1} and $\mathbf{K}_{\theta_{nl}}$, respectively.

Before the assembly into the state-space form the structural stiffness, $\mathbf{K}_s$ lumped in Eq. 2 is considered to consist of linear and non-linear parts described in Equations 6 and 7 as follows:

$$\mathbf{K}_s(w, \theta) = \underbrace{\mathbf{K}_{s_1}\{\mathbf{K}_{w_1}, \mathbf{K}_{\phi_1}, \mathbf{K}_{\theta_1}, \mathbf{K}_{\beta_1}\}}_{\text{linear, augmented eq. (2)}} + \underbrace{\mathbf{K}_{s_{nl}}(\mathbf{K}_w(w), \mathbf{K}_\theta(\theta))}_{\text{non-linear, eq. (6), and (7)}} \tag{8}$$

The non-linear parts of the stiffness matrices, can be solved by discretizing and recomputing the model in a linear form at specific time intervals. The resulting combined stiffness is assembled into a state-space form using Eq. (1).

2. Actuator dynamics and uncertainties

Manufacturing imperfections not only introduce uncertainties about the structural characteristics of a wing design, but only uncertainties related to functional structures such as the actuation system. In particular, when the system is complex and modular, each actuator may be characterized by a different degree of uncertainty and non-linearity. In the general definition of the non-linear aeroelastic system in Eq.12 the actuator uncertainty can be linked to the input u, the control effectiveness matrix $\mathbf{B}$ and flap stiffness $\mathbf{K}_\beta$. Typically, the actuator dynamics can be modeled by a second-order system, which is analogous to a mass-spring-damping system. To parametrically adjust the damping and stiffness parameters, a parameter k is chosen, with the following relationship:

$$\mathbf{K}_\beta = \mathbf{K}_f k^2, \quad \mathbf{C}_\beta = \mathbf{C}_f k \tag{9}$$

Here the matrices $\mathbf{K}_f$ and $\mathbf{C}_f$ represent the actuator stiffness and damping matrices. The quadratic relationship in Eq. (9) ensures that the natural frequency of the actuator dynamics is scaled proportionally, while the damping ratio is kept invariant[19].

It is not trivial to fully characterize actuator uncertainties in complex systems, however, a widely adopted first-order approach in the aeroelasticity domain is a free-play model which described a dead-band between commanded and actual actuator input [20]:

$$\tau = f(t, u) = \begin{cases} k_1(u - u_{f_-}), & \text{if } u < u_{f_-} \\ k_2(u - u_{f_+}), & \text{if } u > u_{f_+} \\ 0, & \text{otherwise} \end{cases} \tag{10}$$

Here k_1 and k_2 are positive scalar values representing linear slopes and u_{f_+} describe the free-play dead-band. In a more challenging scenario, the input u produced by the actuator is not only defined by the commanded input, u_c but also its velocity $\dot{u}_c$ [21, 22]:

$$\dot{\tau} = f(\tau, u, \dot{u}) \begin{cases} k_1 \dot{u}, & \text{if } \dot{u} < 0 \text{ and } \tau = k_1(u - u_{f_-}) \\ k_2 \dot{u}, & \text{if } \dot{u} > 0 \text{ and } \tau = k_2(u - u_{f_+}) \\ 0, & \text{otherwise} \end{cases} \tag{11}$$

Downloaded by Technische Universiteit Delft on January 5, 2024 | http://arc.aiaa.org | DOI: 10.2514/6.2024-0832

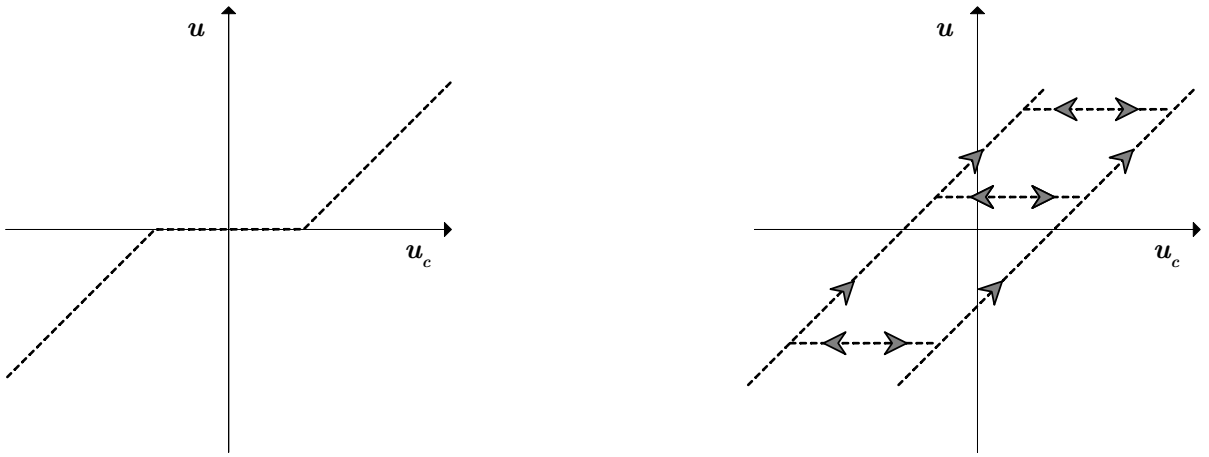

(a) Free-play deadband. **(b) Backlash non-linearity.**

Fig. 6 Illustration of actuator uncertainties described by free-play and backlash phenomena.

Such phenomenon, characterizing dependency on the time history of the commanded signal, known as a backlash, was investigated previously for the SmartX-Alpha demonstrator [4, 5]. The two types of actuator uncertainties are depicted in Fig. 6 [4, 5].

As with the geometric-nonlinearity described in Sec. III.B.1, the actuator uncertainty related to the input u is computed in a discrete-time simulation.

C. Control design

To stabilize the non-linear dynamics of the aeroservoelastic wing model, the system is controlled by SDRE optimal control method. The objective of the SDRE controller is to stabilize the system as optimally as possible concerning the objective function J and bring the initial states back to equilibrium when a state-dependent system is subject to disturbance or an initial input. The SDRE must do so while the model changes due to previous states, previous input, and time. The general state-dependent dynamics of the aeroelastic model can be described as follows:

$$\dot{\mathbf{x}} = \underbrace{(\mathbf{A} + \mathbf{x}_w \mathbf{A}_{nl})\mathbf{x}}_{\mathbf{A}_n} + \underbrace{(\mathbf{B} + \mathbf{B}_{nl})\mathbf{u}}_{\mathbf{B}_n} + \mathbf{B}_g \alpha_g \tag{12}$$

$$\mathbf{y} = \mathbf{C}\mathbf{x} + \mathbf{D}\mathbf{u} \tag{13}$$

Where $\mathbf{A}, \mathbf{B}, \mathbf{B}_g, \mathbf{C}, \mathbf{D}$ are the system dynamic matrices, $\mathbf{u}$ is the input vector with the flap angles, $\mathbf{x}_w$ the state vector describing the nodal displacements (heave), $\mathbf{A}_{nl}$ and $\mathbf{B}_{nl}$ are the state-dependent portion of the dynamics, and α_g is the gust angle of attack input defined in Eq. (5) and added to the system as a disturbance.

In the described dynamics is assumed that the non-linearity arises from: (i) geometric non-linearities in structural stiffness and damping induced by imperfections and uncertainties in the structural system (ii) actuator non-linearities induced by backlash and uncertainties of the actuation system as discussed in Sec. III.B.

More specifically the geometric non-linearity, represented by the structural stiffness $\mathbf{K}_{s_{nl}}$ is tied to $\mathbf{A}_{nl}$ and the actuator non-linearity is tied to the control effectiveness matrix $\mathbf{B}_{nl}$. In a discrete simulation scenario, these non-linearities discussed, are (pre) computed and assembled into the state-space form (Eq.12) using the couplings described in Equations (1) and (2). It is noteworthy to mention that the combined damping matrix augmented to the actuator dynamics is tied to the combined stiffness matrix quadratically as assumed in the definition given by Eq. 9.

For a discrete simulation scenario, to solve and feedback the time-varying system matrices at discrete time steps, the system is modeled in single integrator form.

The gain matrix is obtained to minimize the objectives of interest, namely: the wing root shear force F_w, the wing root bending moment M_ϕ, and the wing tip displacement w_t. The state feedback law minimizes the quadratic cost

Downloaded by Technische Universiteit Delft on January 5, 2024 | http://arc.aiaa.org | DOI: 10.2514/6.2024-0832

function, which for SDRE is defined in its simplest form as:

$$J(\mathbf{x}_0, u) = \frac{1}{2}\int_0^\infty \left(\mathbf{x}^T\mathbf{Q}\mathbf{x} + \mathbf{u}^2\mathbf{R}\mathbf{u}\right) \mathrm{d}t \tag{14}$$

Here, the weight matrices $\mathbf{Q}$ and $\mathbf{R}$ are positive definite matrices that penalize the cost of deviation of the states from zero and the cost of actuation, respectively.

In this particular type of control design, $\mathbf{Q}$ is often chosen as $\mathbf{C}^\mathsf{T}\mathbf{C}$ and $\mathbf{R}$ matrix is often chosen as identity matrix $\mathbf{I}_n$, with $n = 10$. Hence, the second part of the equation can be simplified to u^2 instead of $u^T Ru$.

The SDRE gain is calculated by solving the following Riccati equation [23]:

$$\mathbf{P}_{t+1}\mathbf{An(x)_t} + \mathbf{An(x)_t}\mathbf{P}_{t+1} - \mathbf{P}_{t+1}\mathbf{Bn(x,u)}_t\mathbf{R}^{-1}\mathbf{Bn(x,u)}_t^T\mathbf{P}_{t+1} = 0 \tag{15}$$

The above equation is a minimization problem, centered on finding the state feedback gain matrix, $\mathbf{K} = \mathbf{R}^{-1}\mathbf{B}^\mathsf{T}\mathbf{S}$, required to calculate the stabilizing input to the system at each time step:

$$\mathbf{u}_{t+1} = -\mathbf{K}(\mathbf{x}, \mathbf{An}, \mathbf{Bn}, t)_{t+1} \cdot \mathbf{x} \tag{16}$$

For SDRE this is evaluated as:

$$\mathbf{u}_{t+1} = -\mathbf{R}^{-1}\mathbf{Bn}_t\mathbf{P}_{t+1}\mathbf{x}_t \tag{17}$$

Note that the control effectiveness and the state vector are taken from the previous time step. In a practical implementation using a Simulink model, this can be achieved by a memory block. The equations 17 and 15 are evaluated at each time step. As seen, the gain $\mathbf{K}(\mathbf{x}, \mathbf{An}, \mathbf{Bn}, t)_{t+1}$ needed to compute the stabilizing input, $\mathbf{u} = -\mathbf{K} * \mathbf{x}$, is a function time-varying and state-dependent system matrices $\mathbf{x}_t, \mathbf{An}(\mathbf{x})_t, \mathbf{Bn}(\mathbf{x})_t$ and state vector $\mathbf{x}_t$.

The yielding closed-loop system dynamics are:

$$\dot{\mathbf{x}} = \mathbf{Ax} + \mathbf{Bu} + \mathbf{B}_g\alpha_g = \underbrace{(\mathbf{A} - \mathbf{BK})}_{\mathbf{A_{clp}}}\mathbf{x} + \mathbf{B}_g\alpha_g \tag{18}$$

It is noteworthy that the gust is unknown to the controller. The SDRE assumes that full-state feedback is available. In a real-life system, when full-state feedback is not available the states can be estimated using Kalman filters and sensor fusion(e.g., from cameras, gyros).

IV. Numerical Experiments

To assess the capabilities of the SDRE control approach, and its suitability for application to a state dependent aeroservoelastic systems, two numerical experiments have been set up. The first experiment describes the stabilization for a state dependent sample model using a highly non-linear canard-type aircraft configuration. The second experiment discusses the impact of non-linearities in the actuator dynamics to gust load alleviation of a non-linear aeroservoelastic SmartX-Neo model.

A. Sample model

The non-linear aircraft model investigated is a highly maneuverable aircraft designed by Garrard et al. [24]. The state vector x contains, the deviation of velocity from the trim condition (units 100m/s), the deviation of angle of attack from the trim condition (rad), the pitch rate (rad/s), the flight path angle (rad), and the deviation of canard control flap. The input to the system is the flap angle of the canard in radians.

$$\mathbf{x}(t) = \begin{bmatrix} \Delta V & \Delta\alpha & \dot{p} & \dot{\gamma} & \Delta\delta_{\text{canardmeas}} \end{bmatrix} \tag{19}$$

The parameters of the systems matrices at time step 0 in (level flight) are listed in Appendix B.

In the above equation, the system is represented as quadratically nonlinear in state variables, also a non-linear quadratic coupling is added to the control effectiveness $\mathbf{B}_n$ as explained in [24]. The nonlinearity is assumed to be affine in control hence a non-linear state space, $\mathbf{A}_n$,$\mathbf{B}_n$ can be obtained from the following summation of state matrices:

Downloaded by Technische Universiteit Delft on January 5, 2024 | http://arc.aiaa.org | DOI: 10.2514/6.2024-0832

$$\dot{\mathbf{x}}(t) = \underbrace{(\mathbf{A_0} + x_2\mathbf{A}_{nl})\mathbf{x}}_{\mathbf{A}_n} + \underbrace{(\mathbf{B}_1 + u\mathbf{B}_2)u}_{\mathbf{B}_n} \tag{20}$$

The instability of the system is shown in 8b. It arises from both the instability in $A0$ and the non-linear coupling of the angle of attack. The system can become highly unstable due to coupling the quadratic non-linear coupling of the control effectiveness matrix B with the input.

B. Aeroservoelastic model and simulation set-up

To conduct the simulation experiment, a state-space aeroelastic dynamic model was established as described in Sec III.C. The scope of the simulation was limited to testing the hypotheses presented in IV.C. Two scenarios, where the actuator dynamic were impacted by (i) free-play and (ii) backlash, and the impact on the GLA performance was studied in both scenarios.

Therefore, the model was simplified by assuming no geometric non-linearity, $\mathbf{A}_{nl}$ in the system. Since the free-play and backlash non-linearity, described in equations 10 and 11 in Sec. III.B.2, cannot be directly added through a linear $\mathbf{B}_{nl}$ matrix, the model was modified as follows:

$$\dot{\mathbf{x}} = \mathbf{A}\mathbf{x} + \mathbf{B}_g\alpha_g + \mathbf{B}_f f(\mathbf{u}_c) \tag{21}$$

$$\mathbf{y} = \mathbf{C}\mathbf{x} + \mathbf{D}\mathbf{u} \tag{22}$$

Where the system matrices are as defined in Sec III.C, $\mathbf{u}_c$ is the commanded flap signal, and actual flap input signal $\mathbf{u}$ is obtained by adopting either the free-play ($\mathbf{u}_c = f(t, \mathbf{u}_c)$) or backlash ($\mathbf{u}_c = f(t, \mathbf{u}_c, \dot{\mathbf{u}}_c)$) models described in Sec. III.B.2.

The non-linearities in this case did not arise from the state dependency of the system as with the sample model, rather from uncertainty added to the actuator dynamics. This uncertainty was assumed to be unknown to the controller. The close loop control was designed to minimize the, the shear force F_w, root bending moment M_ϕ, wing torsion M_θ and the tip displacement w_t. The, $\mathbf{Q}$ is chosen as $\mathbf{C}^\mathsf{T}\mathbf{C}$, while $\mathbf{R}$ is chosen as an identity matrix $\mathbf{I}_n$, with $n = 10$. As with a previous study using LQR, it was assumed that the gust signal was an unknown disturbance and the full state feedback is available [7].

Each scenario was simulated for the duration of 1.2 seconds, where a variable sampling time was adopted in Simulink with a relative tolerance of $1e-5$ and maximum step-size of 0.04.

C. Hypotheses

In this study, the analysis shall focus on studying the effect of systems imperfection towards Gust Load Alleviation (GLA) performance. More precisely, two types of actuator uncertainty shall be introduced to make the system imperfect, free-play and backlash. Considering the assumption and constraints made in the preceding section, the following two hypotheses are formulated:

1) the first hypothesis is that actuator uncertainty will reduce gust load alleviation performance;
2) the second hypothesis is that actuator uncertainty will have a destabilizing effect on the system;

V. Results and Discussions

In this section, the analysis of the design and the results of the simulation experiment with the state dependent sample model and the aeroservoelastic models, defined in Sections IV.A and IV.B shall be discussed. Firstly, the performance of the SDRE controller is discussed for the state dependent sample model defined in Sec. V.A. Secondly, the impact of actuator non-linearities and uncertainties are discussed in Sec. V.B on the load alleviation performance using the free-play and the backlash model presented in Sec. III.B.2. Lastly, the impact of damping and stiffness variation of the actuator dynamics combined with uncertainty is discussed in Sec. V.B.3.

A. Results sample model

The SDRE controller is designed according to the methodology and the objective function described in Sec. III.C, while the objective aims to minimize the deviation from an initial state and reduce the actuation effort.

Downloaded by Technische Universiteit Delft on January 5, 2024 | http://arc.aiaa.org | DOI: 10.2514/6.2024-0832

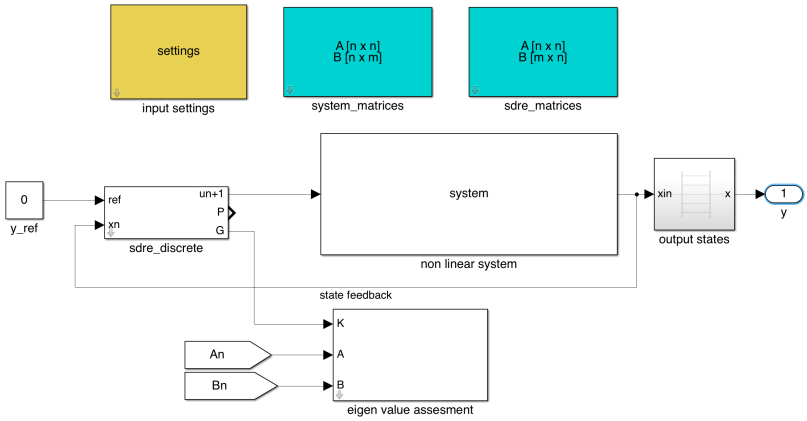

Fig. 7 Overview Simulink model.

In the context of the non-linear system, the task of the controller in the sample case is to stabilize all states of the non-linear system, $\mathbf{x}(t)$, while a large angle of attack input (e.g. due to gust) of 25 degree ($25 \cdot (\pi/180)$ rad as x_{20}) causes the system to perturb from the trim state. The choice of the Q and R matrices are given in the appendix.

To solve the system at each time step and recalculate the stabilizing feedback on the time-varying system matrices, the system is modeled in single integrator form. This is seen in the main system block, Fig. 7. The system is modeled in Simulink and simulated for 10 seconds.

Figures 8b and 8a, and 9 and 9a show the SDRE-stabilized versus open-loop system response. The stabilization is achieved by reevaluating the control input $\mathbf{u} = -\mathbf{K} * \mathbf{x}$ at discrete time intervals. The gain $\mathbf{K}(\mathbf{x}, \mathbf{An}, \mathbf{Bn}, t)_{t+1}$, calculated for the next time step, is a function time-varying and state-dependent system matrices $\mathbf{x}_t, \mathbf{An}(\mathbf{x})_t, \mathbf{Bn}(\mathbf{x})_t$ and state vector $\mathbf{x}_t$.

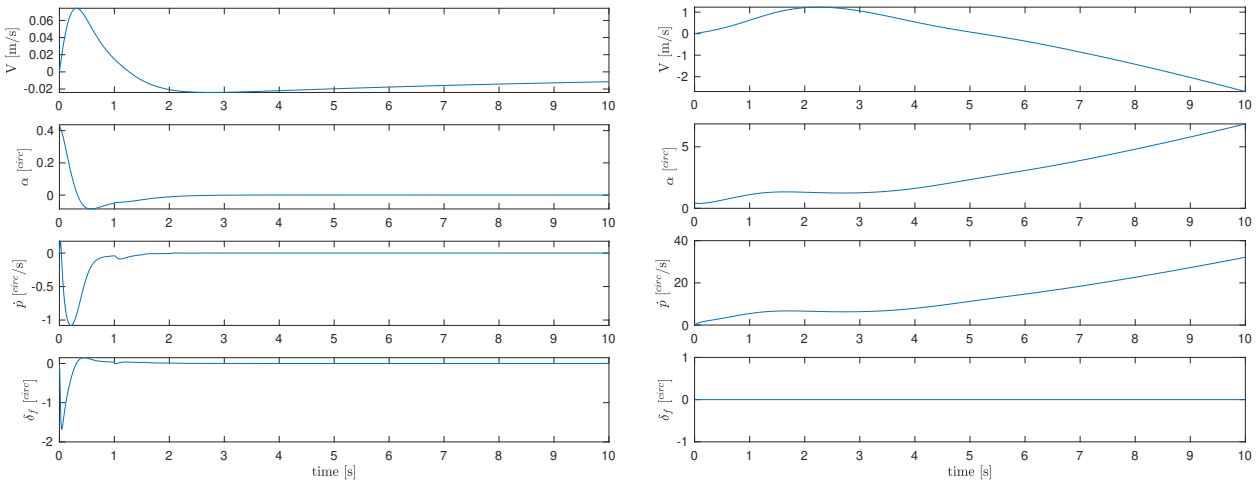

(a) Response of controlled stable system. **(b) Response of open-loop unstable stable system.**

Fig. 8 SDRE stabilized system. It's seen how the response is stabilized and the coefficients of the system matrices settle.

The Figure sequence in 10 shows snapshots of system poles and zeros at discrete intervals between 0-10 seconds. As seen, the poles travel towards the RS (Right-Hand side) indicating higher instability in the dominant pole related to the angle of attack coupling with flap input. Furthermore, the state vector becomes unstable as shown in Fig. 8b. The stable system on the other hand ($\mathbf{A}_n - \mathbf{B}_n \cdot \mathbf{K}_{SDRE}(\mathbf{x}, t)$) stabilizes the system by the computed SDRE feedback gain $\mathbf{K}_{SDRE}$ and return to initial equilibrium. The latter is indicated by the travel of the poles towards LH (Left-Hand side) and the stabilized time traces shown in Fig. 8a.

Downloaded by Technische Universiteit Delft on January 5, 2024 | http://arc.aiaa.org | DOI: 10.2514/6.2024-0832

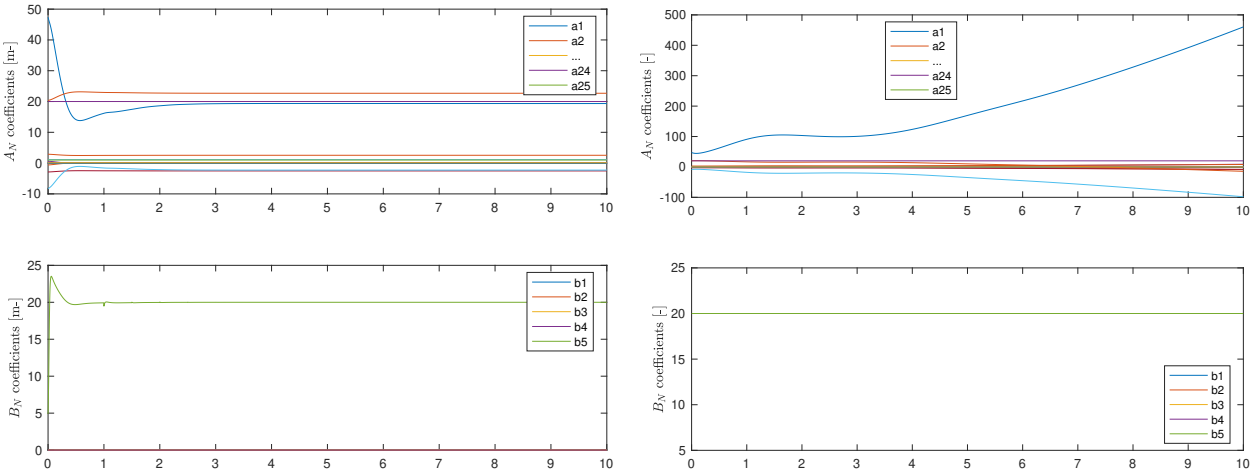

(a) Variation of model coefficients with time (stable) **(b) Variation of model coefficients with time (unstable)**

Fig. 9 Change of model coefficients of table (left) and unstable (right) system. The B does not change in the open loop system since the input is $u = 0$.

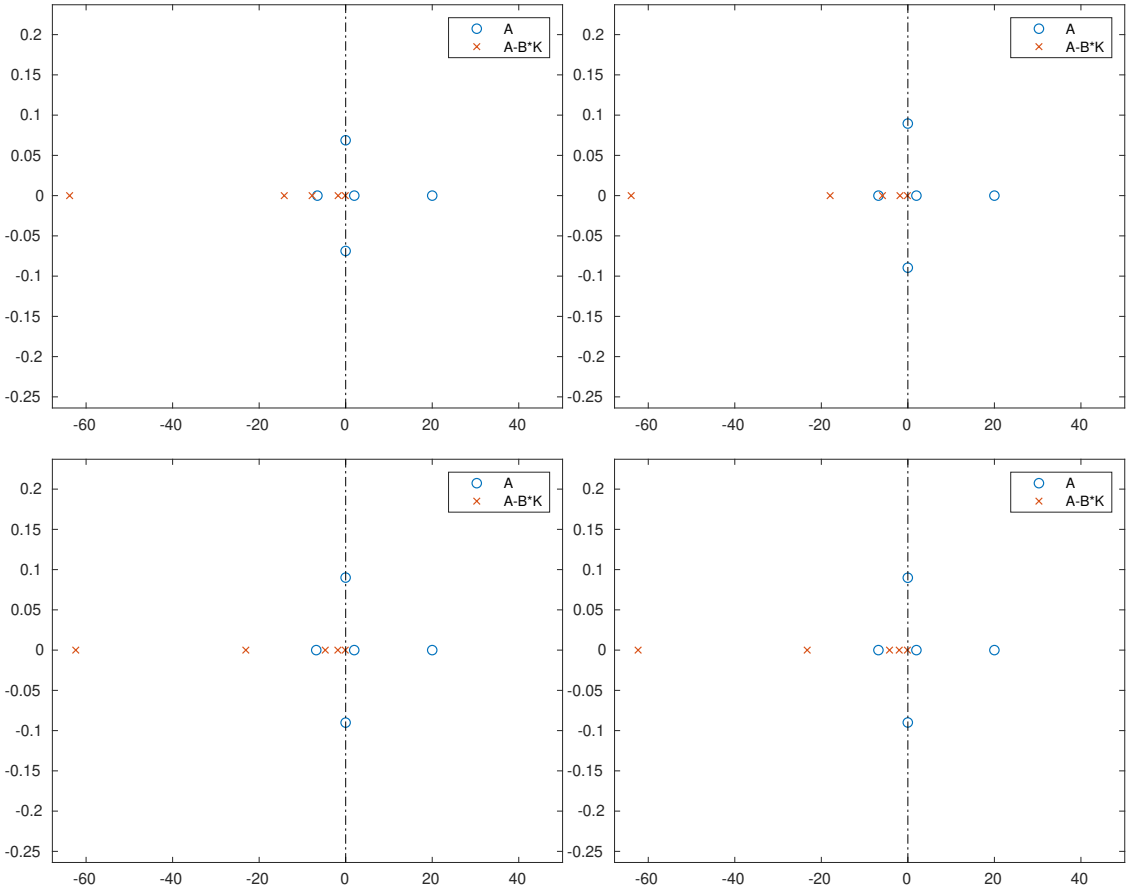

Fig. 10 Comparison of change in eigenvalues for unstable and stable systems with SDRE gain feedback. As the input grows, the open loop system becomes more unstable, and the dominant unstable related to alpha shifts towards RS, while the stable system towards the LS.

Downloaded by Technische Universiteit Delft on January 5, 2024 | http://arc.aiaa.org | DOI: 10.2514/6.2024-0832

B. Impact of actuator uncertainties

The actuator uncertainties can have a significant performance on load alleviation effectiveness and for some systems in most adverse cases lead to instabilities. A visual representation of both free-play and backlash was presented described in Sec III.B.2, Figures 11a and 11b were simulated with a sinusoidal tracking signal. The time trace shown in Figures 11a shows the commanded compared to output flap signal when filtered through both types of uncertainty models. As seen, the free-play model shown in the left figure mainly results in lead-lag effect for a commanded signal of 10 degree of flap deflection (blue dotted line). The dead-band parameters for the simulation are $1, 3, 5$ degrees, respectively. Backlash, shown in the right figure, is characterized by a lag effect and flattening of the commanded peak deflection. The latter is a more complex phenomenon, as the output depends on both the magnitude and the rate of the commanded angle u_c. In the latter simulation, the dead-band angle parameters for the backlash model are similarly $1, 3, 5$ degrees.

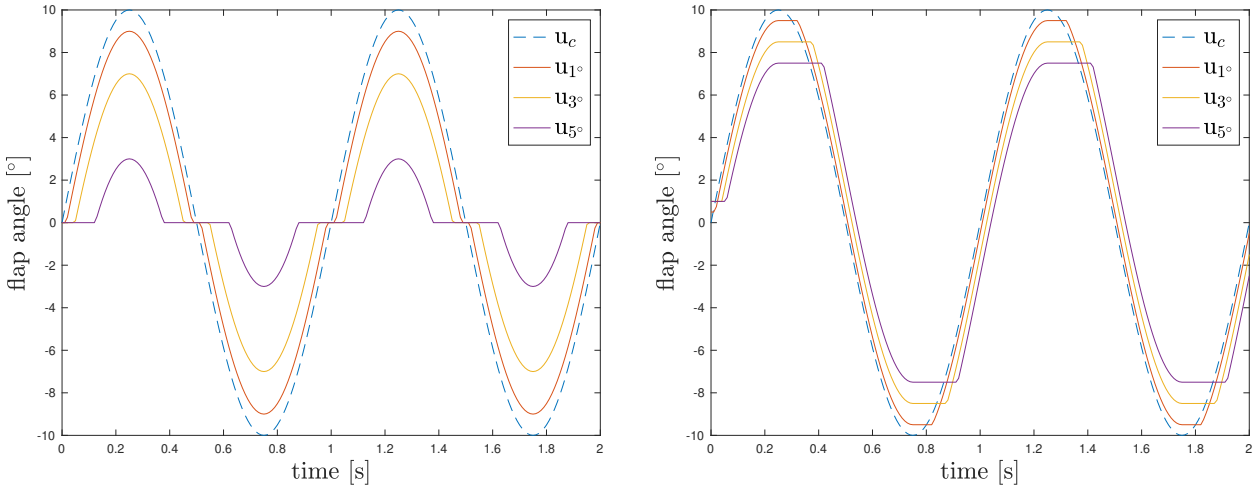

(a) Free-play dead-band response. **(b) Backlash non-linearity.**

Fig. 11 Illustration of actuator response subject to free-play and backlash uncertainty.

In the following sections, the impact of free-play and backlash was evaluated on the aeroelastic wing model described in Sec III and closed loop control design described in Sec III.C.

1. Free-play

The impact of free-play on the model was studies with varying levels of severity expressed in degrees of dead-band, namely $1, 3, 5$ and 7 degrees. Figure 12 shows the closed loop response to free-play for the root bending moment M_ϕ, wing torsion M_θ and the tip displacement w_t. The color indicates varying degrees of free-play introduced to the system as an input signal u. The blue line corresponds to no-free play; the green line, to free-play of 7 degrees. Going from left to right, it is apparent that increasing severity of free-play results in less effective load alleviation. For reference, the open-loop response is shown in App. Appendix C in Fig. 21 with the addition of the shear force F_w. While open-loop performance is worse by a significant degree, nevertheless it is evident that actuation originating from a phenomenon such as free-play will significantly impact the performance of the controller. Moreover, observing the torsion response in the rightmost figure for free-play of higher degrees, it can be assumed that higher levels of free-play are likely to destabilize the system more. This is seen by the oscillatory response of the wing torsion towards the end of the simulation (green curve). It is likely that more complex phenomena such as backlash can be more destabilizing, as is discussed in Sec. V.B.2.

A closer look at the destabilizing effect is given in Figures 13a and 13b showing the wing bending and torsion, and the actuator inputs respectively. In Fig. 13b the actuator inputs of the most outboard actuator are shown in terms of the commanded signal u_c, originating from the controller and the resulting input signal u_f after free-play of varying degrees. As seen the, the transient free-play signal u_f introduced to the system is showing increasingly higher peaks at higher dead-band degrees before settling to bounded oscillations towards the end of the gust onset. The collective actuation command for 5 degree of free-play for all actuators is shown in Fig. 18a. These findings agree with the

Downloaded by Technische Universiteit Delft on January 5, 2024 | http://arc.aiaa.org | DOI: 10.2514/6.2024-0832

Downloaded by Technische Universiteit Delft on January 5, 2024 | http://arc.aiaa.org | DOI: 10.2514/6.2024-0832

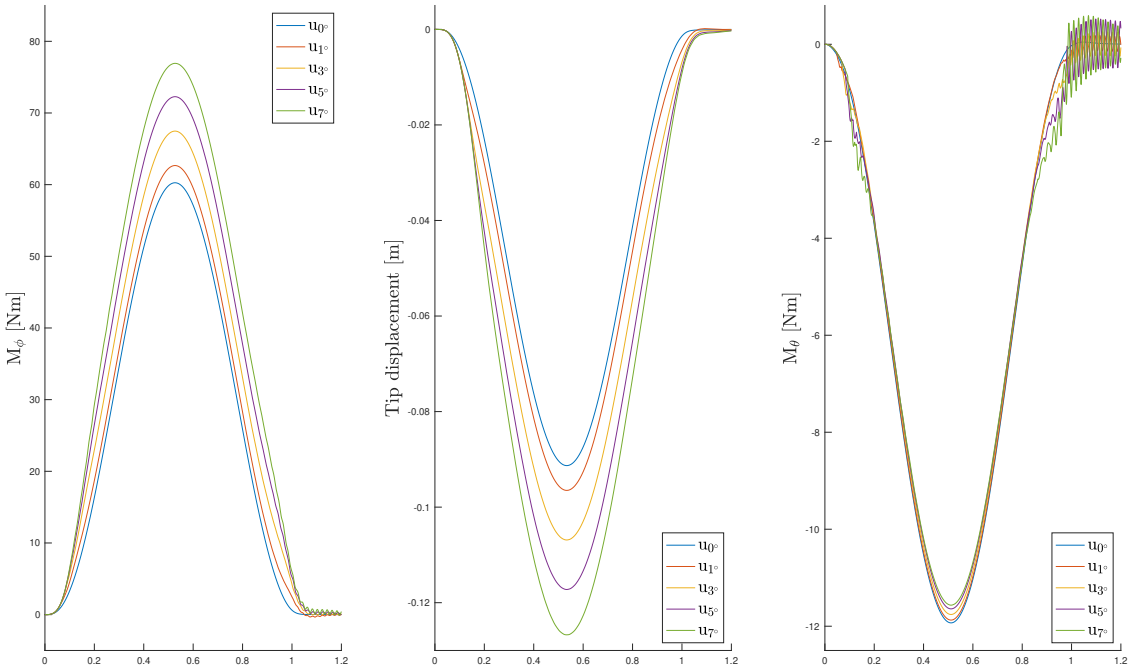

Fig. 12 Closed-loop response comparisons with free-play.

hypotheses stated earlier that the actuator uncertainties are likely to have a destabilizing effect and a reduction in load alleviation performance.

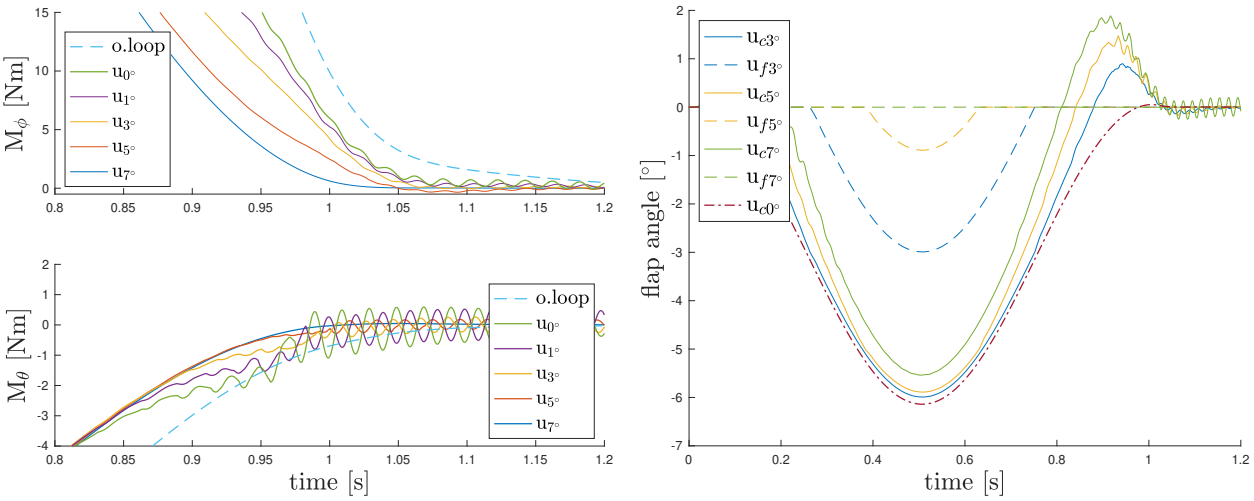

(a) Destabilization of the closed-loop response. **(b) Comparison of actuator commands.**

Fig. 13 Comparison responses to various degrees of free-play.

2. Backlash

Similar to the free-play, the impact of backlash was studies with varying levels of severity expressed in degrees of dead-band, namely 1, 3, 5 and 7 degrees. The closed loop response to backlash is shown in Fig. 14, for the root bending moment M_ϕ, wing torsion M_θ and the tip displacement w_t. The open-loop response can be found in App. Appendix C Fig. 22 with the addition of the shear force F_w. Demonstrated in Fig. 14 across varying severities, backlash does not

particularly manifest in reduced load alleviation performance, but rather adds significant destabilization of the wing torsion moment. The wing bending moment response shown in the right most figure exhibits an oscillatory signature of up to 10 Nm across varying severity levels.

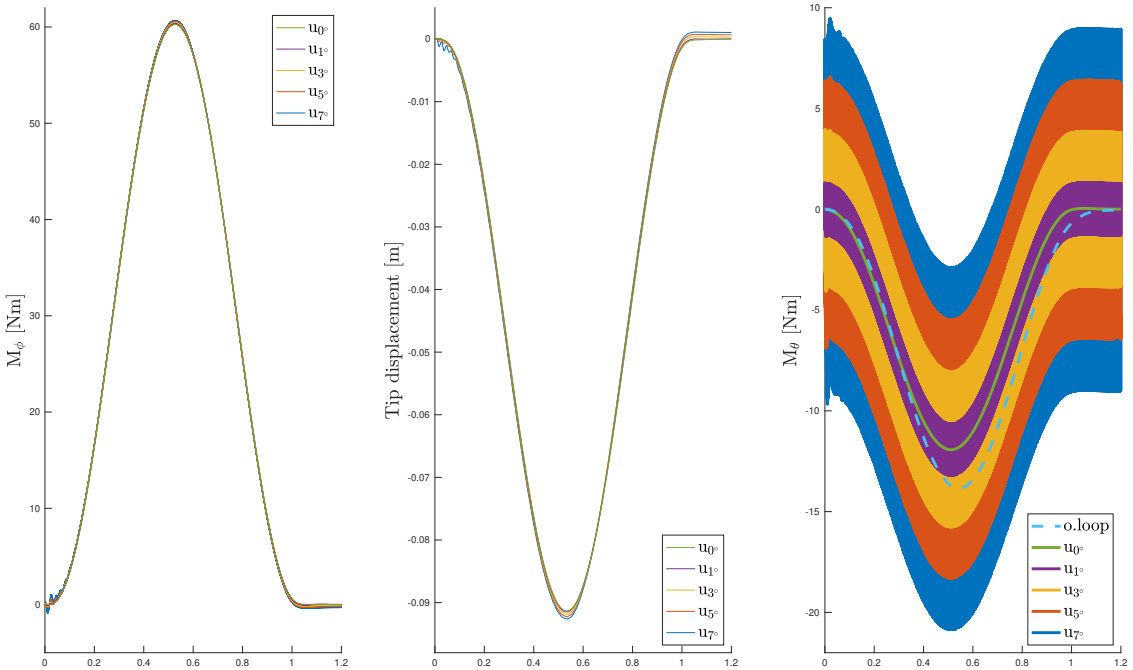

Fig. 14 Closed-loop response comparisons with backlash.

The destabilization becomes more apparent on the zoomed transient response shown in Figures 15a and 15b, where high frequency oscillation are observed in the wing torsion at the onset of the gust disturbance. From the actuation input shown in Fig. 15b the destabilizing effect can be seen to originate from the actuation input. Overall it is apparent that for this system, wing torsion is more sensitive to actuation input and in particular will be impacted by the higher degree of uncertainty for either backlash or free-play shown in Figures 13b and 15b.

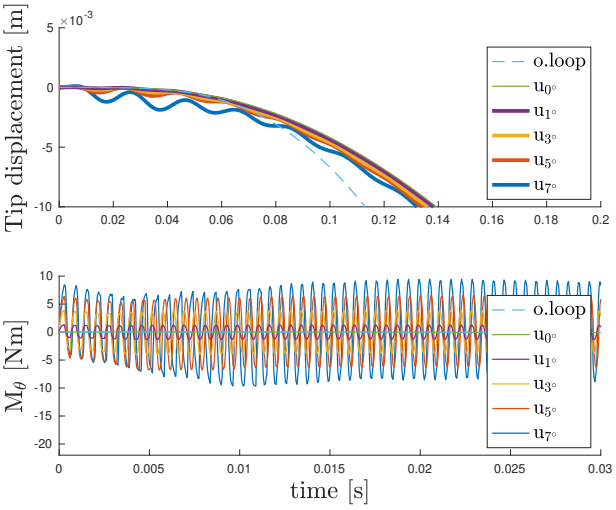

(a) Destabilization of the closed-loop response.

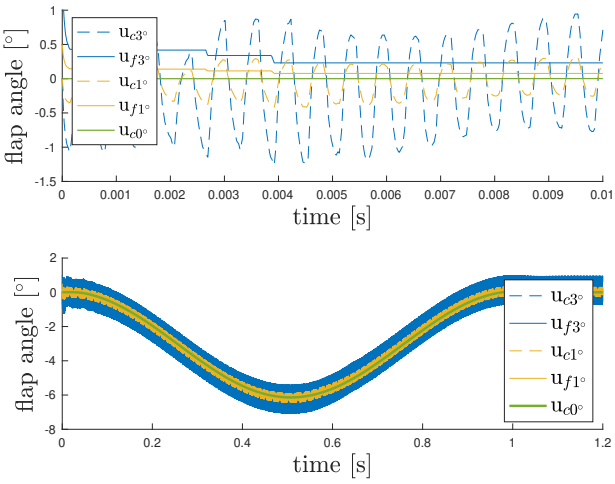

(b) Comparison of actuator commands.

Fig. 15 Comparison responses to various degrees of backlash.

Downloaded by Technische Universiteit Delft on January 5, 2024 | http://arc.aiaa.org | DOI: 10.2514/6.2024-0832

3. Impact of actuator damping and stiffness combined with uncertainty

In a previous study, the effect of damping and stiffness variation of the actuator dynamics of the aeroservoelastic model were studied [19]. The study demonstrated that as the bandwidth of the actuator is increased ($k < 1$), the controller was able to react more effectively to the gust disturbance and exhibited better performance. However, no actuator uncertainty was assumed for the latter study. It is noteworthy to understand how the higher bandwidth system would fare with free-play or backlash present.

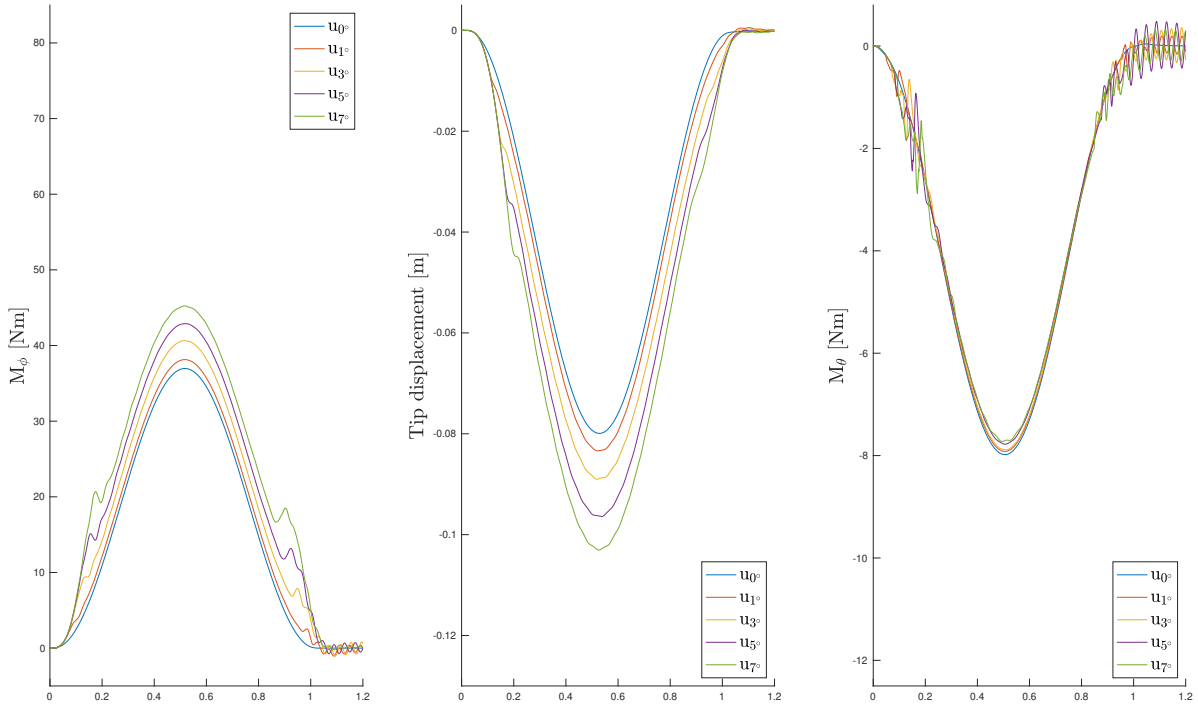

Fig. 16 Closed-loop response comparisons with free-play and actuator scaling parameter $k = 0.5$.

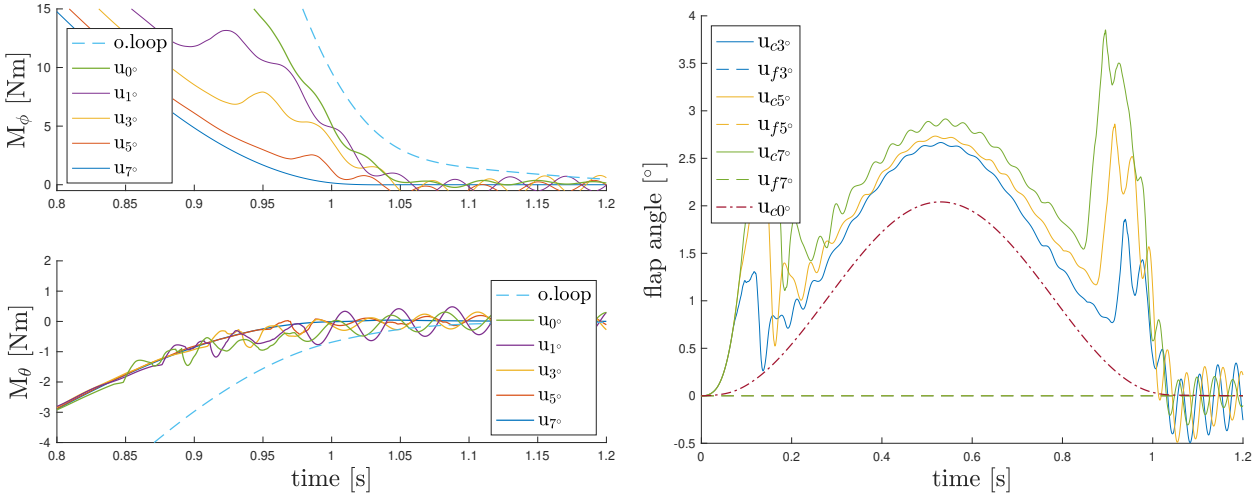

(a) Destabilization of the closed-loop response. **(b) Comparison of actuator commands.**

Fig. 17 Comparison responses to various degrees of free-play and actuator scaling parameter $k = 0.5$.

To evaluate the impact of the actuator uncertainty, the scaling parameter, as described in Sec. III.B.2 was set to

Downloaded by Technische Universiteit Delft on January 5, 2024 | http://arc.aiaa.org | DOI: 10.2514/6.2024-0832

$k = 0.5$ and the altered model was re-run with the previous settings for free-play and backlash. It is clear from the closed loop response shown in Figures. 16 and 17a that relaxing the scaling parameter has a destabilizing effect when combined with free-play. This is particularly evident when comparing the oscillation towards the edges with the relatively smooth response of the shear force, Fig. 12 for the nominal system ($k = 1$). From Fig. 17b it is clear that the source of the destabilization lies in a more disturbed feedback signal compared to Fig. 13b. Furthermore, it is observed that a higher degree of free-play causes an increasingly larger deviation of the actuation command from the perfect system (red dotted line).

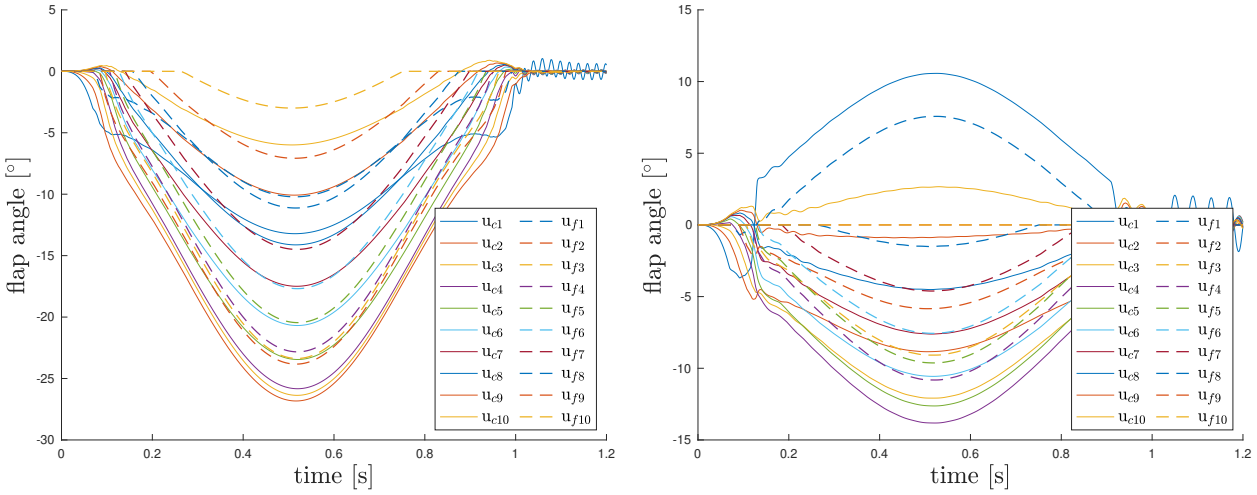

(a) Actuator commands for $k = 1$. **(b) Actuator commands for $k = 0.5$.**

Fig. 18 Collective actuator commands due to free-play of 5 degrees for varying scaling.

While for backlash the lower scaling has not significantly altered the transient behavior of the close loop response (App. Appendix C in Fig. 25), a larger band of uncertainty is observed in the actuator input in Fig. 17b compared to Fig. 13b. Collectively, these findings agree with the hypothesis stated earlier that the actuator uncertainties are likely to have a destabilizing effect.

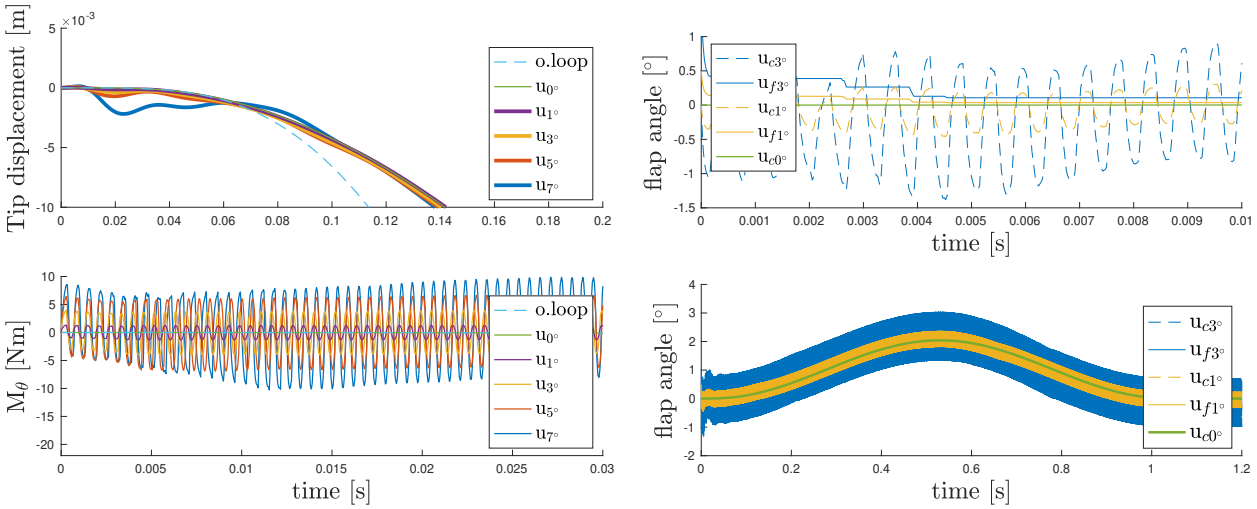

(a) Destabilization of the closed-loop response. **(b) Comparison of actuator commands.**

Fig. 19 Comparison responses to various degrees of backlash and actuator scaling parameter $k = 0.5$.

Downloaded by Technische Universiteit Delft on January 5, 2024 | http://arc.aiaa.org | DOI: 10.2514/6.2024-0832

VI. Conclusion and Recommendation

The ability of SDRE to stabilize a highly non-linear system was demonstrated by running a test case example of the aircraft configuration. The design of the SDRE objective was then discussed, tailored to a multi-objective stabilization and gust load alleviation problem of an uncertain non-linear aeroelastic system subject to gust disturbance. In particular, the effect of dynamics and uncertainties were studies in this paper by means of non-linearities introduces in the system through free-play and backlash. The general observation were that higher severity of the free-play and backlash dead-band resulted in lower effectiveness in load alleviation performance in addition to destabilization of the with closed loop control performance. In particular, while free-play led to lower load alleviation performance, backlash led to larger destabilization effect across the wing torsion for this system. The main observation is that the wing torsion, generally operating at higher frequencies, is more likely to be destabilized by higher-frequency oscillation resulting from actuation imperfections. Finally, the variation of stiffness and damping characteristics were studies in combination with actuation uncertainties and bandwidth. Collectively, these findings suggested that actuator uncertainties are likely to have a more destabilizing effect, particularly when coupled to a more responsive system. It is recommended to further study the impact of non-linearities resulting from not only the actuation system, but also from the structural and aerodynamic impact added to the systems' response.

Downloaded by Technische Universiteit Delft on January 5, 2024 | http://arc.aiaa.org | DOI: 10.2514/6.2024-0832

References

[1] Lentink, D., Müller, U. K., Stamhuis, E. J., De Kat, R., Van Gestel, W., Veldhuis, L. L., Henningsson, P., Hedenström, A., Videler, J. J., and Van Leeuwen, J. L., "How swifts control their glide performance with morphing wings," *Nature*, Vol. 446, No. 7139, 2007, pp. 1082–1085. https://doi.org/10.1038/nature05733.

[2] Bomphrey, R. J., Henningsson, P., and Hedenstro, A., "Efficiency of Lift Production in Flapping and Gliding Flight of Swifts," *PLoS ONE*, Vol. 9, No. 2, 2014. https://doi.org/10.5061/dryad.cn252.

[3] JEX, H., and CULICK, F., "Flight control dynamics of the 1903 Wright Flyer," *12th Atmospheric Flight Mechanics Conference*, American Institute of Aeronautics and Astronautics, Reston, Virigina, 1985, pp. –. https://doi.org/10.2514/6.1985-1804, URL http://arc.aiaa.org/doi/10.2514/6.1985-1804.

[4] Wang, X., Mkhoyan, T., Mkhoyan, I., and De Breuker, R., "Seamless Active Morphing Wing Simultaneous Gust and Maneuver Load Alleviation," *Journal of Guidance, Control, and Dynamics*, Vol. 44, No. 9, 2021, pp. 1649–1662. https://doi.org/10.2514/1.G005870.

[5] Sun, B., Mkhoyan, T., Van Kampen, E., Breuker, R., and Wang, X., "Vision-Based Nonlinear Incremental Control for A Morphing Wing with Mechanical Imperfections," *IEEE Transactions on Aerospace and Electronic Systems*, Vol. 58, No. 6, 2022, pp. 5506–5518. https://doi.org/10.1109/TAES.2022.3175679.

[6] Bhoir, N., and Singh, S. N., "Control of unsteady aeroelastic system via state-dependent Riccati equation method," *Journal of Guidance, Control, and Dynamics*, Vol. 28, No. 1, 2005, pp. 78–84.

[7] Li, D., Guo, S., and Xiang, J., "Aeroelastic dynamic response and control of an airfoil section with control surface nonlinearities," *Journal of Sound and Vibration*, Vol. 329, No. 22, 2010, pp. 4756–4771.

[8] Strano, S., and Terzo, M., "A SDRE-based tracking control for a hydraulic actuation system," *Mechanical Systems and Signal Processing*, Vol. 60, 2015, pp. 715–726.

[9] Mkhoyan, T., Thakrar, N. R., De Breuker, R., and Sodja, J., "Design and Development of a Seamless Smart Morphing Wing Using Distributed Trailing Edge Camber Morphing for Active Control," *AIAA Scitech 2021 Forum*, 2021, p. 0477.

[10] Mkhoyan, T., Thakrar, N. R., De Breuker, R., and Sodja, J., "Design of a Smart Morphing Wing Using Integrated and Distributed Trailing Edge Camber Morphing," *ASME 2020 Conference on Smart Materials, Adaptive Structures and Intelligent Systems*, American Society of Mechanical Engineers, 2020, pp. –. https://doi.org/10.1115/smasis2020-2370, URL https://asmedigitalcollection.asme.org/SMASIS/proceedings/SMASIS2020/84027/Virtual,Online/1090388.

[11] Werter, N. P., Sodja, J., Spirlet, G., and De Breuker, R., "Design and experiments of a warp induced camber and twist morphing leading and trailing edge device," *24th AIAA/AHS Adaptive Structures Conference*, 2016. https://doi.org/10.2514/6.2016-0315, URL http://arc.aiaa.org.

[12] Deperrois, A., *XFLR5 Theoretical overview*, 2021. URL http://www.xflr5.tech/xflr5.htm.

[13] Systèmes, D., *ABAQUS/CAE Theory Guide, Version 6.19*, Dassault Systèmes, 2019.

[14] Drela, M., *XFOIL: an analysis and design system for low Reynolds number airfoils.*, 54), Berlin, Germany, Springer-Verlag, 1989, Springer-Verlag Wien, 1989.

[15] De Breuker, R., Binder, S., and Wildschek, A., "Combined active and passive loads alleviation through aeroelastic tailoring and control surface/control system optimization," *AIAA Aerospace Sciences Meeting, 2018*, Vol. 1, No. 210059, 2018. https://doi.org/10.2514/6.2018-0764, URL https://arc.aiaa.org/doi/pdf/10.2514/6.2018-0764.

[16] Theodorsen, T., "General theory of aerodynamic instability and the mechanism of flutter (NACA-TR-496)," *National Advisory Committee for Aeronautics, Langley Field, VA*, 1949. URL http://www.tree-o-life.org/ARO202/naca-report-496.pdf.

[17] Leishman, J. G., "Subsonic unsteady aerodynamics caused by gusts using the indicial method," *Journal of Aircraft*, Vol. 33, No. 5, 1996, pp. 869–879. https://doi.org/10.2514/3.47029, URL http://arc.aiaa.org/doi/10.2514/3.47029.

[18] Lee, K. W., and Singh, S. N., "Robust finite-time continuous control of an unsteady aeroelastic system," *Journal of Guidance, Control, and Dynamics*, Vol. 41, No. 4, 2018, pp. 978–986.

[19] Mkhoyan, T., Wang, X., and De Breuker, R., "Aeroelastic Wing Demonstrator with a Distributed and Decentralized Control Architecture," *AIAA SCITECH 2022 Forum*, 2022, pp. 1–20. https://doi.org/10.2514/6.2022-1551, aIAA SCITECH 2022 Forum ; Conference date: 03-01-2022 Through 07-01-2022.

[20] Gold, P., and Karpel, M., "Reduced-size aeroservoelastic modeling and limit-cycle-oscillation simulations with structurally nonlinear actuators," *Journal of Aircraft*, Vol. 45, No. 2, 2008, pp. 471–477. https://doi.org/10.2514/1.28933.

[21] Frampton, K. D., and Clark, R. L., "Experiments on control of limit-cycle oscillations in a typical section," *Journal of Guidance, Control, and Dynamics*, Vol. 23, No. 5, 2000, pp. 956–960. https://doi.org/10.2514/2.4638.

[22] Campos, J., Lewis, F. L., and Selmic, R., "Backlash compensation in discrete time nonlinear systems using dynamic inversion by neutral networks," *Proceedings - IEEE International Conference on Robotics and Automation*, Vol. 2, No. 2, 2000, pp. 1289–1295. https://doi.org/10.1109/robot.2000.844776.

[23] Beeler, S. C., "State-Dependent Riccati Equation Regulation of Systems with State and Control Nonlinearities," Tech. rep., NASA, 2004. URL http://www.sti.nasa.gov.

[24] Garrard, W. L., Enns, D. F., and Antony Snell, S., "Nonlinear feedback control of highly manoeuvrable aircraft," *International Journal of Control*, Vol. 56, No. 4, 1992, pp. 799–812. https://doi.org/10.1080/00207179208934344.

Downloaded by Technische Universiteit Delft on January 5, 2024 | http://arc.aiaa.org | DOI: 10.2514/6.2024-0832

Appendix A. Planform Parameters

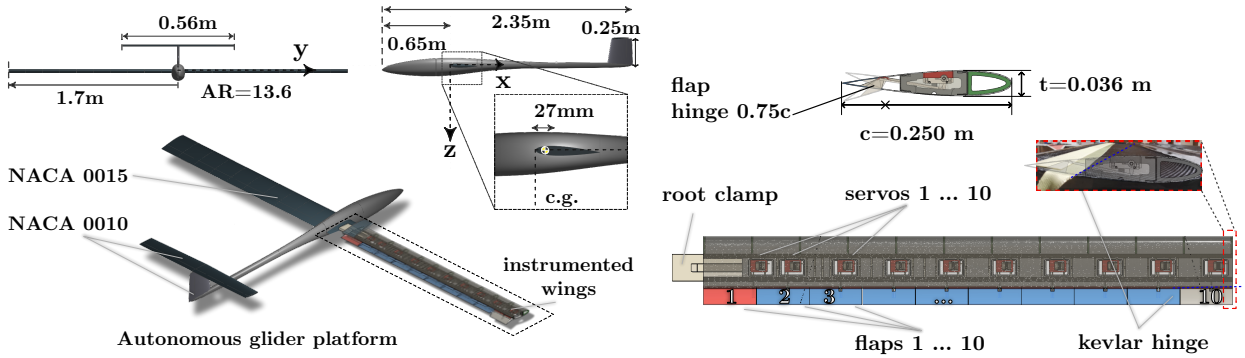

(a) Aircraft planform design. **(b) Wing planform design.**

Fig. 20 Overview of the wing planform design.

Table 1 Planform parameters.

Item		Symbol	Value	Unit
Wing aspect ratio		AR	13.6	[-]
Wing span		b_w	3.4	[m]
Wing loading		b_w	6.706	[kg/m^2]
Fuselage length		L_f	2.345	[m]
Elevator span		b_e	0.56	[m]
Vertical stabilizer span		b_s	0.25	[m]
Wing chord	(NACA 0015)	c_w	0.25	[m]
Elevator chord (root,tip)	(NACA 0010)	c_e	(1.67,1.45)	[m]
Vertical stabilizer chord (root,tip)	(NACA 0010)	c_s	(0.24,0.19)	[m]
Elevator incidence angle		α_i	-4	[$\circ$]
Fuselage position	x (w.r.t. wing)	x_f	-0.645	[m]
c.g. position	x (w.r.t. wing)	x_{cg}	0.027	[m]
Neutral point	x (w.r.t. wing)	x_{np}	0.305	[m]
Total mass		W_t	5.7	[kg]
Payload mass		W_p	1.5	[kg]

Downloaded by Technische Universiteit Delft on January 5, 2024 | http://arc.aiaa.org | DOI: 10.2514/6.2024-0832

Appendix B. System Matrices sample case model

The system matrices of the sample model with the non-linear canard configuration are given below [24].

$$\mathbf{A_0} = \begin{bmatrix} -0.0443 & 1.1280 & 0.0 & -0.0981 & 0.0 \\ -0.0490 & -2.5390 & 1.0 & 0.0 & -0.0854 \\ -0.0730 & 19.32 & -2.2700 & 0.0 & 22.6834 \\ 0.0490 & 2.5390 & 0.0 & 0.0 & 0.0854 \\ 0.0 & 0.0 & 0.0 & 0.0 & 20.0 \end{bmatrix} \tag{23}$$

$$\mathbf{A_{nl}} = \begin{bmatrix} -0.2317 & 0.0 & 0.0 & 0.0 & 0.0 \\ -1.2760 & -0.7922 & 0.0 & 0.0 & 0.0206 \\ 0.1020 & 64.2940 & -13.9710 & 0.0 & -5.4167 \\ 1.2760 & 0.7922 & 0.0 & 0.0 & -0.0206 \\ 0.0 & 0.0 & 0.0 & 0.0 & 0.0 \end{bmatrix} \tag{24}$$

$$\mathbf{B_1} = \begin{bmatrix} 0.0 & 0.0 & 0.0 & 0.0 & 20.0 \end{bmatrix}^T \tag{25}$$

$$\mathbf{B_2} = \begin{bmatrix} 0.0 & 0.0 & 0.0 & 0.0 & 2.0 \end{bmatrix}^T \tag{26}$$

$$\mathbf{Q} = \begin{bmatrix} 100 & 0 & 0 & 0 & 0 \\ 0 & 10 & 0 & 0 & 0 \\ 0 & 0 & 10 & 0 & 0 \\ 0 & 0 & 0 & 100 & 0 \\ 0 & 0 & 0 & 0 & 10 \end{bmatrix} \tag{27}$$

$$R = 1 \tag{28}$$

$$\mathbf{x0} = \begin{bmatrix} 0 & 25 \cdot (\pi/180) & 0 & 0 & 0 \end{bmatrix}^T \tag{29}$$

Appendix C. Responses open and closed loop systems

Downloaded by Technische Universiteit Delft on January 5, 2024 | http://arc.aiaa.org | DOI: 10.2514/6.2024-0832

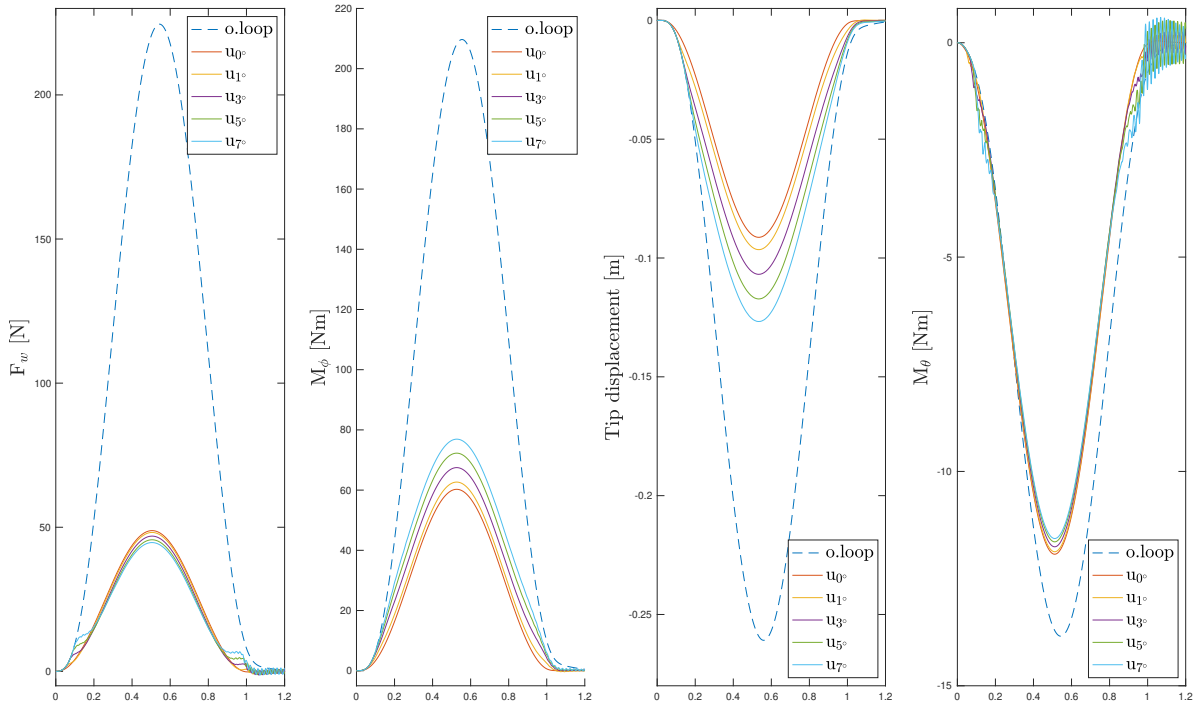

Fig. 21 Open and closed-loop response comparisons with free-play and actuator scaling parameter $k = 0.5$.

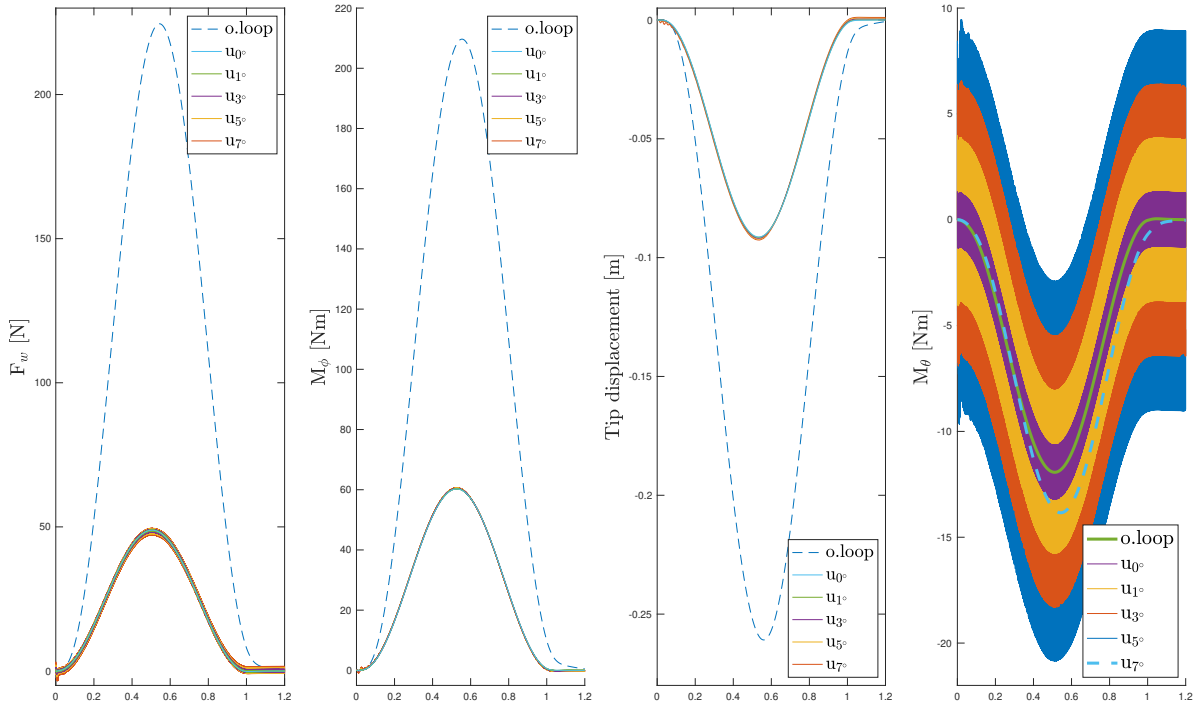

Fig. 22 Open and closed-loop response comparisons with backlash and actuator scaling parameter $k = 0.5$.

Downloaded by Technische Universiteit Delft on January 5, 2024 | http://arc.aiaa.org | DOI: 10.2514/6.2024-0832

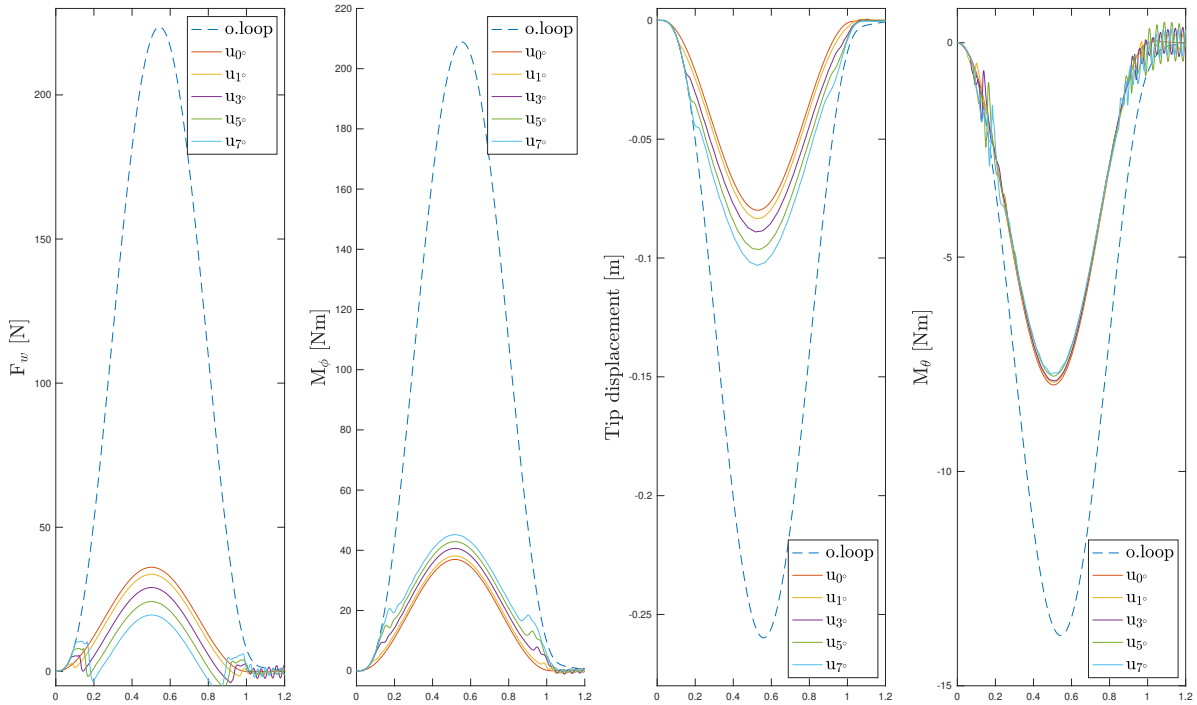

Fig. 23 Open and closed-loop response comparisons with free-play and actuator scaling parameter $k = 0.5$.

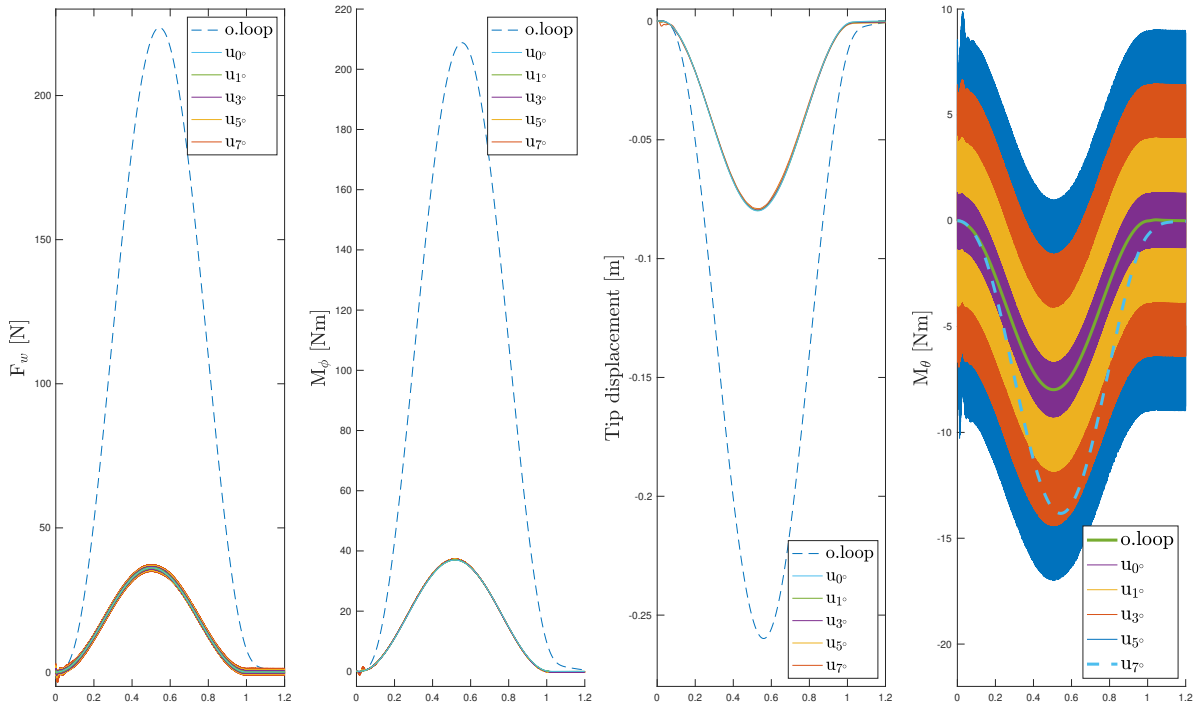

Fig. 24 Open and closed-loop response comparisons with backlash and actuator scaling parameter $k = 0.5$.

Downloaded by Technische Universiteit Delft on January 5, 2024 | http://arc.aiaa.org | DOI: 10.2514/6.2024-0832

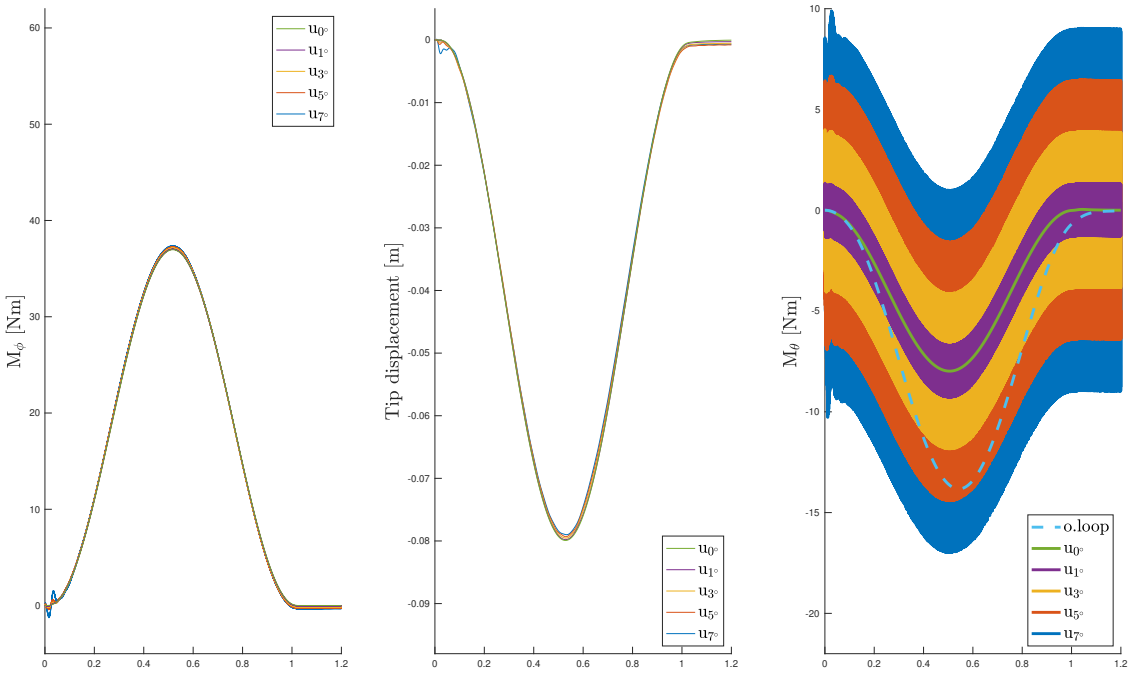

Fig. 25 Closed-loop response comparisons with backlash and actuator scaling parameter $k = 0.5$.